

Tautomeric mixture coordination enables efficient lead-free perovskite LEDs

<https://doi.org/10.1038/s41586-023-06514-6>

Received: 11 January 2023

Accepted: 2 August 2023

Published online: 9 August 2023

 Check for updates

Dongyuan Han^{1,9}, Jie Wang^{1,9}, Lorenzo Agosta², Ziang Zang¹, Bin Zhao¹, Lingmei Kong³, Haizhou Lu^{4,5}✉, Irea Mosquera-Lois², Virginia Carnevali², Jianchao Dong¹, Jianheng Zhou¹, Huiyu Ji¹, Lukas Pfeifer⁴, Shaik M. Zakeeruddin⁴, Yingguo Yang^{6,7}, Bo Wu⁸, Ursula Rothlisberger², Xuyong Yang³✉, Michael Grätzel⁴✉ & Ning Wang¹✉

Lead halide perovskite light-emitting diodes (PeLEDs) have demonstrated remarkable optoelectronic performance^{1–3}. However, there are potential toxicity issues with lead^{4,5} and removing lead from the best-performing PeLEDs—without compromising their high external quantum efficiencies—remains a challenge. Here we report a tautomeric-mixture-coordination-induced electron localization strategy to stabilize the lead-free tin perovskite TEA_2SnI_4 (TEAI is 2-thiopheneethylammonium iodide) by incorporating cyanuric acid. We demonstrate that a crucial function of the coordination is to amplify the electronic effects, even for those Sn atoms that aren't strongly bonded with cyanuric acid owing to the formation of hydrogen-bonded tautomeric dimer and trimer superstructures on the perovskite surface. This electron localization weakens adverse effects from Anderson localization and improves ordering in the crystal structure of TEA_2SnI_4 . These factors result in a two-orders-of-magnitude reduction in the non-radiative recombination capture coefficient and an approximately twofold enhancement in the exciton binding energy. Our lead-free PeLED has an external quantum efficiency of up to 20.29%, representing a performance comparable to that of state-of-the-art lead-containing PeLEDs^{6–12}. We anticipate that these findings will provide insights into the stabilization of Sn(II) perovskites and further the development of lead-free perovskite applications.

Tin (Sn) has been regarded as a viable replacement for lead in metal halide perovskites because it has a similar valence electron configuration and ionic radius as lead^{13–15}. Nonetheless, the external quantum efficiencies (EQEs) of Sn-based perovskite light-emitting diodes (PeLEDs) are lower than those of their lead-based counterparts^{16–18}. Most strategies adopted to improve Sn-based PeLEDs have been focusing on inhibiting the oxidation of Sn^{2+} by introducing Sn compensators¹⁹ and reducing agents²⁰. However, only limited improvement has been achieved because these techniques cannot effectively remove the defects in the resultant Sn perovskite films. Furthermore, the residual chemical agents often destroy the orderliness of the crystal lattice of Sn perovskites, resulting in Anderson localization²¹, which is detrimental to the optoelectronic properties. Morphological control¹⁸ and solvent engineering¹⁷ methods have also been developed to increase the EQE of Sn-based PeLEDs by up to 5.4%. The low EQE of Sn-PeLEDs implies a limited understanding of the intrinsic instability of Sn^{2+} , and more in-depth studies are needed to further enhance both EQE and stability of Sn-based PeLEDs.

The facile oxidation of Sn^{2+} fundamentally originates from the delocalized $5s^2$ lone-pair electrons, which can cause detrimental p-type

self-doping^{13,22}. A recent study¹⁶ demonstrated a chemical coordination strategy to reduce Sn^{4+} that boosted both EQE (up to 5%) and the stability of Sn-based PeLEDs. Moreover, another study²³ reported localized electron engineering for improving Sn-based perovskite solar cells. We were motivated to establish strong chemical coordination with Sn^{2+} to inhibit electron delocalization, boosting Sn-based PeLEDs. Cyanuric acid (CA) is a typical delocalized aromatic compound that possesses low electronegativity and strong electron-donating ability^{24,25}, favouring the interaction with Sn^{2+} . Notably, ab initio molecular dynamics (AIMD) simulations show that a mixture of CA tautomers is key to forming strong chemical bonds on the Sn perovskite surface.

Configuration of CA on TEA_2SnI_4

To understand the chemical coordination interaction between CA and two-dimensional TEA_2SnI_4 perovskite, we performed Fourier transform infrared (FTIR) spectroscopy measurements. Figure 1a and Supplementary Fig. 1 show that the stretching vibration of C=N at $1,678 \text{ cm}^{-1}$ for the CA molecule shifted to $1,697 \text{ cm}^{-1}$ for the cyanuric-acid-treated

¹College of Physics, Jilin University, Changchun, China. ²Laboratory of Computational Chemistry and Biochemistry, Institute of Chemical Sciences and Engineering, École Polytechnique Fédérale de Lausanne (EPFL), Lausanne, Switzerland. ³Key Laboratory of Advanced Display and System Applications of Ministry of Education, Shanghai University, Shanghai, China. ⁴Laboratory of Photonics and Interfaces, Institute of Chemical Sciences and Engineering, École Polytechnique Fédérale de Lausanne (EPFL), Lausanne, Switzerland. ⁵Key Laboratory of MEMS of Ministry of Education, School of Integrated Circuits, Southeast University, Nanjing, China. ⁶Shanghai Synchrotron Radiation Facility (SSRF), Zhangjiang Lab, Shanghai Advanced Research Institute, Chinese Academy of Sciences, Shanghai, China. ⁷School of Microelectronics, Fudan University, Shanghai, China. ⁸Guangdong Provincial Key Laboratory of Optical Information Materials and Technology and Institute of Electronic Paper Displays, South China Academy of Advanced Optoelectronics, South China Normal University, Guangzhou, China. ⁹These authors contributed equally: Dongyuan Han, Jie Wang. ✉e-mail: haizhou.lu@epfl.ch; yangxy@shu.edu.cn; michael.gratzel@epfl.ch; ningwang@jlu.edu.cn

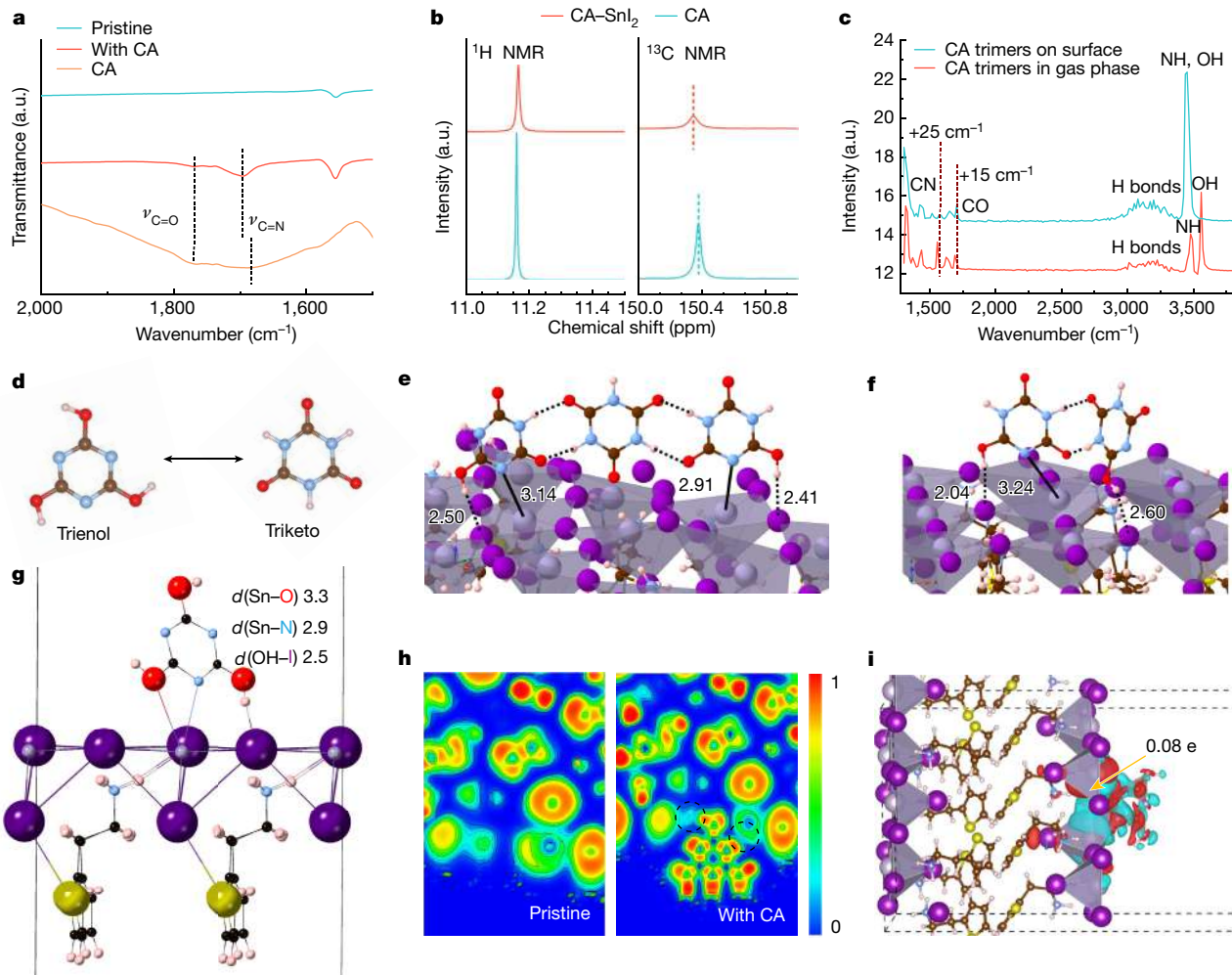


Fig. 1 | Interaction and configuration of CA and TEA_2SnI_4 perovskite. **a**, FTIR spectra of TEA_2SnI_4 with and without CA, and pure CA. **b**, ^1H NMR (left) and ^{13}C NMR (right) spectra for pure CA and the composite CA– SnI_2 . **c**, Vibrational power spectra of the most stable trimer configuration in vacuum and adsorbed on the perovskite surface. **d**, Trienol and triketo forms of CA. **e,f**, The most stable configurations for the tautomeric CA trimer (**e**) and dimer (**f**) bonded to the Sn perovskite surface. The distances are in ångström (Å). Colour code:

Sn, grey; I, purple; S, yellow; C, brown; H, pink; O, red; N, blue. **g**, Configuration and characteristic interactions of CA on the TEA_2SnI_4 perovskite surface. Colour code: Sn, grey; I, purple; S, yellow; C, black; H, pink; O, red; N, blue. **h**, Electron localization function images of pristine perovskite (left) and perovskite with CA (right), which were obtained in systems with an iodide vacancy. **i**, Charge density difference between the Sn perovskite and CA. a.u., arbitrary units.

Sn perovskite, suggesting a strong C=N bond, which arises because of the interaction of C=N and Sn perovskite. This is consistent with the electrostatic potential of the enol form of the CA molecule (Extended Data Fig. 1), indicating that the region near the nitrogen atom in the triazine ring has a high electron density. It could act as the site for donating lone-pair electrons to coordinate with Sn(II) (ref. 26). The appearance of the characteristic vibration peak of C=O at $1,775\text{ cm}^{-1}$ for CA and CA-treated Sn perovskite implies the coexistence of keto form—that is, the presence of a tautomeric mixture of CA, which will be discussed later.

Subsequently, ^1H NMR measurements were carried out. Chemical shift of the resonance signal of CA (Fig. 1b) indicates the formation of hydrogen bonds in the form of $\text{N}=\text{C}-\text{OH}\cdots\text{I}^-$ (ref. 16). The broad resonance signal of SnI_2 -CA suggests that the CA molecule is immobilized by the $\text{N}=\text{C}-\text{OH}\cdots\text{I}^-$ hydrogen bonds, which prevents the migration of I^- . A similar phenomenon was also observed in ^{13}C NMR spectroscopy, which further confirms the strong interaction between CA and Sn(II). The FTIR and NMR spectroscopy results agreed well with the X-ray photoelectron spectroscopy (XPS) measurements (Supplementary Fig. 2), which show a chemical shift of the Sn 3d and I 3d XPS peaks after introducing CA into the Sn perovskite.

AIMD simulations were used to investigate the configuration of CA on the perovskite surface, we observed the formation of CA dimers and trimers consisting of mixed enol and keto forms (Extended Data Fig. 2 and Supplementary Video 1). The possibility of a strong C=N...Sn²⁺ coordination of the enol form leads to a partial surface-induced tautomerization of the thermodynamically more stable keto form. This tautomeric mixture is stabilized by the strong intermolecular N-H...O/H...N hydrogen bonds^{27,28}. We also carried out a computation of the vibrational spectra of various types of surface-absorbed CA molecule (Fig. 1c). When the trimer is adsorbed on the surface, a blue shift of 25 cm^{-1} and 15 cm^{-1} (with respect to the same isolated trimer) is presented for C–N ($1,650\text{ cm}^{-1}$) and C–O ($1,775\text{ cm}^{-1}$) stretch vibrations, which is in good agreement with the experimental FTIR spectroscopy measurements. We note the presence of O–H vibrational modes at about $2,900$ – $3,300\text{ cm}^{-1}$ is consistent with the formation of strong hydrogen bonds, a signature of the keto-enol hydrogen-bonded di- and trimers forms.

We conclude that CA molecules on the Sn perovskites are composed of a mixture of keto and enol tautomers that form dimers or trimers (Supplementary Table 1). These ordered complexes are nearly commensurate with the perovskite lattice (Sn–Sn second nearest distance is 1.05 nm , whereas the O–C–N...O–C–N distance of the extreme CA

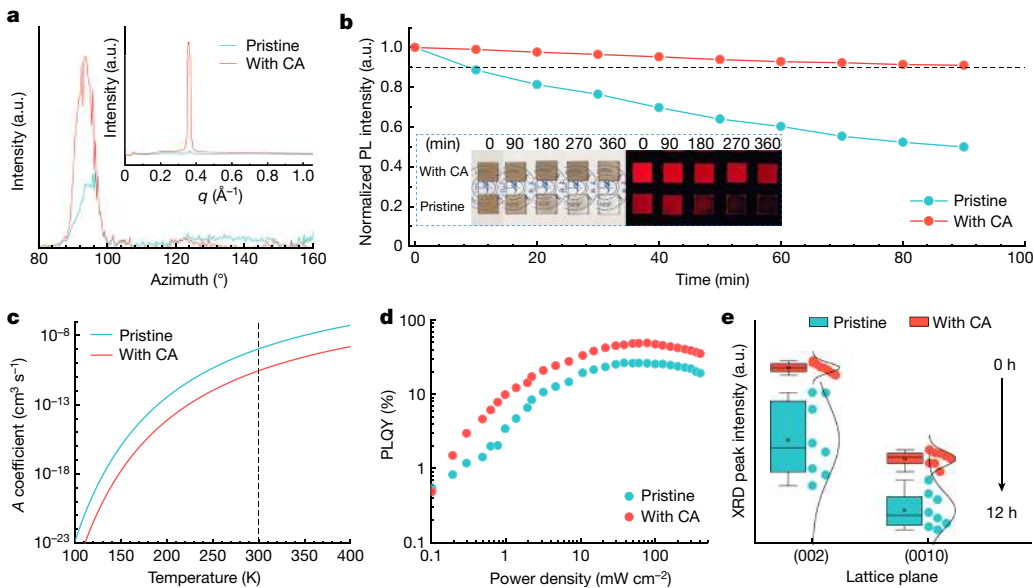


Fig. 2 | Crystallization kinetics and non-radiative recombination evaluation.

a, Intensity curves of GIWAXS patterns along the (002) ring for the samples with and without CA. Inset, integrated intensity of GIWAXS patterns for the samples. **b**, Time-dependent normalized PL intensity measurements for the pristine and the TEA_2SnI_4 film with CA exposed to dry air (20% humidity, room temperature) for 90 min. The horizontal dashed line indicates 90% of the initial normalized PL intensity. Inset, photographs of the samples in air and in the dark

with an excitation wavelength of 365 nm. **c**, Curves of the non-radiative capture coefficient A versus temperature of the Sn perovskites. The vertical dashed line corresponds to room temperature. **d**, Excitation-intensity-dependent PLQI of the Sn perovskite films with and without CA. **e**, The distribution of peak XRD intensity for the pristine sample and sample with CA measured in dry air for 12 h. a.u., arbitrary units.

molecules in the trimer is 1.1 nm) allowing for strong N–Sn coordination augmented by the interaction between OH^- and H-bond (Fig. 1d–g), providing adequate protection of the perovskite surface against Sn(II) oxidation as well as Sn and I^- loss. Beyond surface passivation/protection, the polyfunctional character of CA in combination with its ability to form ordered structures with a well-defined perpendicular orientation of the aromatic ring planes with respect to the surface suggests an additional potential to stabilize grain boundaries by crosslinking different grains through N/O-Sn and H-I interaction. Noticeably, this unique interaction between CA and Sn perovskite is distinctly different from previous reports (Extended Data Fig. 2)^{1,16}.

Structure and stability

To understand how CA could stabilize the Sn perovskite, we performed a Bader analysis. It was found that the Sn electron density becomes more localized on coordination substantially reducing the corresponding Bader volume from around $59\text{--}62 \text{ au}^3$ to 24 au^3 . This effect even extends to nearby surface Sn^{2+} atoms that have only weak interaction with CA ($d(\text{Sn}-\text{O}) = 3.3 \text{ \AA}$, $d(\text{Sn}-\text{N}) = 3.3 \text{ \AA}$), and still experience a clear localization of the Sn charge density (Bader volume of about $45\text{--}56 \text{ au}^3$). Both the coordinating bonds and their localizing effect contribute to the stabilization of surface Sn^{2+} thus preventing Sn(II) oxidation.

Furthermore, the electron localization function was calculated to provide a mapping of the electron cloud in the pristine and the CA-treated Sn perovskite (Fig. 1h). The electron cloud in the dashed region of the CA-treated Sn perovskite indicates strong electron localization of Sn^{2+} . The triketone form of CA also showed similar properties (Extended Data Fig. 1). The effect of CA on electronic properties is further investigated by applying charge density difference (Fig. 1i). Electron transfer between CA and Sn perovskite is evaluated to be 0.08 e⁻, suggesting strong interaction between CA and undercoordinated Sn^{2+} , which inhibits charge transfer from Sn^{2+} to O_2 molecule (Supplementary Table 2)^{29–31}. The planar-averaged charge density difference (Extended Data Fig. 1 and Supplementary Fig. 3) also proves the charge redistribution at the interface, in combination with the negligible change

of dielectric constants, which can benefit the carrier transport and improve electrical conductivity.

Scanning electron microscope images of the TEA_2SnI_4 perovskite with 5% CA showed a smoother surface morphology than the other sample (Extended Data Fig. 3 and Supplementary Fig. 4). Atomic force microscope images further show the flatter film surface in the treated sample. Grazing incidence wide-angle X-ray scattering (GIWAXS) measurements (Fig. 2a, Extended Data Fig. 4 and Supplementary Fig. 5) suggested a highly uniform parallel orientation of the Sn perovskite films^{32,33}. Compared with the pristine, the target film showed more preferred orientation, stronger diffraction intensity and narrower full width at half maximum (FWHM), which implies much more ordered stacking and better crystallinity of the perovskite crystal plates because of the introduction of CA, therefore avoiding Anderson localization³⁴. Moreover, the low- n -phase components of the Sn perovskite films are suppressed effectively with the CA treatment. Such preferentially oriented crystallinity favours efficient carrier injection and prevents ion migration along the vertical direction during device operation³⁵.

Kelvin probe force microscopy measurements indicated that the Sn perovskite film with CA possesses a higher surface potential (Extended Data Fig. 3 and Supplementary Fig. 6), which is mainly because of the reduced number of surface defects³⁶. Calculations of the density of states (Extended Data Fig. 1) showed that iodide vacancy states in the band edge of the Sn perovskite were reduced by CA³⁷, avoiding the presence of undercoordinated Sn^{2+} that aggravates Sn^{2+} oxidation. The suppression of I defects is vital to avoid non-radiative recombination loss in Sn perovskites. We find that the content of I^- substantially increases from 82.4% in the pristine to 97.1% in the treated film (Extended Data Fig. 5 and Supplementary Table 3). The Sn:I ratios in the pristine and the target film were calculated to be 0.25 and 0.23, respectively. These results indicate that CA can prevent the migration of I^- and suppress its evolution to I_2 or I_3^- (ref. 38). Furthermore, we find that the content of Sn is increased by a factor of 1.09 compared with the pristine. Beyond suppressing I and Sn loss, CA prevents Sn^{2+} oxidation, as demonstrated by XPS measurements, which illustrates a decrease in the content of Sn^{4+} from 16.5% in the pristine to 7.6% in the target sample (Extended

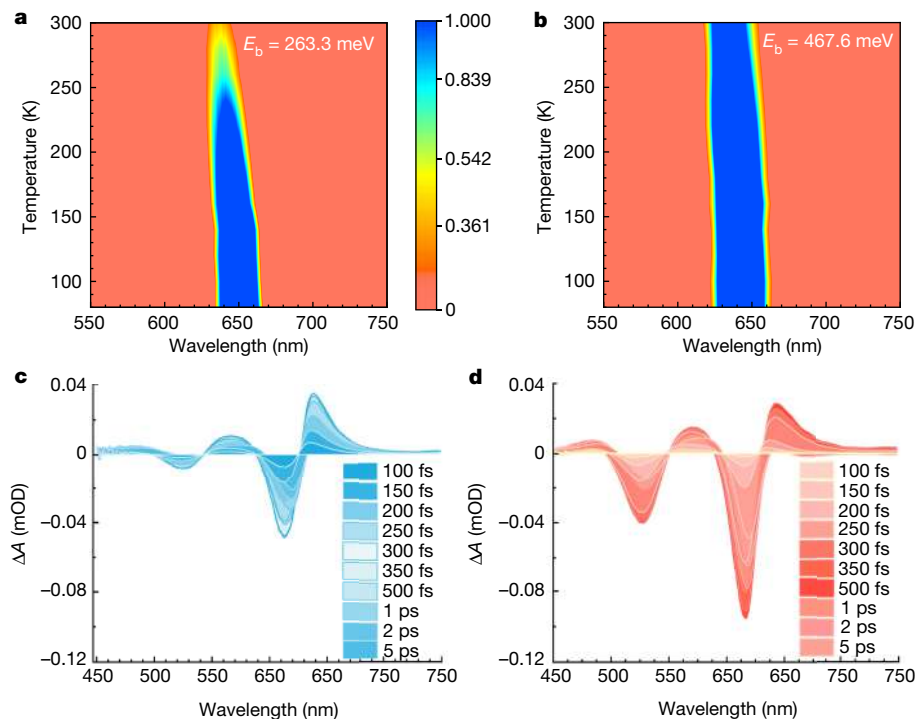


Fig. 3 | Photophysics and carrier dynamics of TEA₂SnI₄ films. **a,b**, Temperature-dependent PL spectra mapping for the pristine film (**a**) and TEA₂SnI₄ film with CA (**b**). **c,d**, Transient absorption (TA) spectra of the pristine film (**c**) and TEA₂SnI₄ film with CA (**d**).

Data Fig. 5). To explain the effect of CA on trap states, we carried out measurements on Urbach energy (E_U) and time-resolved photoluminescence (TRPL) spectroscopy (Extended Data Fig. 6). The E_U value decreased from 137 meV to 85 meV and the average carrier lifetime increased from 1.44 ns to 3.45 ns when CA was introduced. Furthermore, enhanced photoluminescence (PL) intensity is also observed in the CA-treated film.

Generally, the facile oxidation of Sn²⁺ to Sn⁴⁺ and the unstable crystal structures are responsible for undermining the stability of Sn perovskite films^{29,39}. To check the shelf stability of the Sn perovskites in ambient air condition, time-dependent normalized PL measurements were performed (Fig. 2b and Supplementary Figs. 7 and 8). In contrast to the sharp reduction of PL intensity of the pristine with time, the target film retained its 90% initial PL intensity within 90 min. The non-radiative recombination capture coefficient A of the Sn perovskite sample was reduced by more than two orders of magnitude from $1.01 \times 10^{-9} \text{ cm}^3 \text{ s}^{-1}$ to $2.45 \times 10^{-11} \text{ cm}^3 \text{ s}^{-1}$ by introducing CA (Fig. 2c, Extended Data Fig. 6 and Supplementary Fig. 9). This indicates that the CA-treated Sn perovskite is potentially a remarkable luminescent material. Excitation-intensity-dependent photoluminescence quantum yield (PLQY) measurements showed that the PLQYs of the films increase with the excitation intensity to a large extent (Fig. 2d). It is well understood that, as the defect states are gradually filled, radiative bimolecular recombination begins to dominate the luminescence process during this test⁴⁰. Afterwards, the X-ray diffraction (XRD) characterization was carried out, and the patterns of the films with CA showed stronger diffraction intensity and narrower FWHM (Extended Data Fig. 4) than the reference, which is because of the larger crystal size and better crystallinity (Extended Data Fig. 5). Furthermore, the XRD patterns of the films and nanoplates stored in dry air without encapsulation for different time are also presented for detecting the effect of CA on crystal stability of the Sn perovskites (Fig. 2e, Extended Data Fig. 5 and Supplementary Fig. 10). After 720-min storage, the diffraction intensity (002) of the films with CA decreases less than that of the pristine. The reduced non-radiative recombination coefficient and stabilized large crystal act together to improve the stability of the Sn perovskite.

Photophysical properties

As temperature increases (Fig. 3a,b), for the temperature-dependent steady-state PL spectra measurements, the PL intensity of the target film slightly decreased and the corresponding peak position of blue shifted by approximately 5 nm compared with the pristine (16 nm). These results indicate that the thermal quenching of fluorescence caused by non-radiative recombination can be essentially inhibited in the target film by CA coordination⁴¹. We evaluated the exciton binding energy (E_b) of the target film to be 467.6 ± 43.3 meV, which is about twofold higher than that of the pristine (263.3 ± 30.1 meV) (Extended Data Fig. 7). The enlarged E_b of the target film suggests a higher energy threshold for exciton dissociation, making them promising luminescent materials.

Transient-absorption measurements showed two pronounced photo-bleaching peaks at about 615 nm and about 522 nm for both the pristine and the target sample, respectively (Fig. 3c,d and Extended Data Fig. 7), which are attributed to the 1s and 2s excitons⁴². The enhanced transient-absorption signal at the two exciton resonances for the treated sample compared with the pristine (around four times at 2s exciton and twice at 1s exciton) may be attributed to the enhanced Coulombic interaction and excitonic effect because of CA treatment. We notice that within 5 ps after photoexcitation, the exciton bleaching peaks show fast redshift, which is usually recognized as the filling process of the band tail states. The smaller shift of transient bleach further confirmed the reduced band tail states in the treated sample. Furthermore, we analysed the bleach recovery kinetics by fitting the decay curves with a tri-exponential function (Supplementary Fig. 11). The fast decay (τ_1) is attributed to the hot carrier relaxation, convoluted with the fast carrier trapping. The intermediate decay (τ_2) is responsible for the carrier trapping by defects. The treated sample shows a slower defect trapping rate, in agreement with the reduced defect traps through CA coordination-induced electron localization. As a result, the bleach signal for the treated sample displays a higher fraction of long-lived component (slow decay $\tau_3 > 5$ ns) than that of the pristine (slow decay $\tau_3 > 4$ ns), which is attributed to the recombination of photoexcited species.

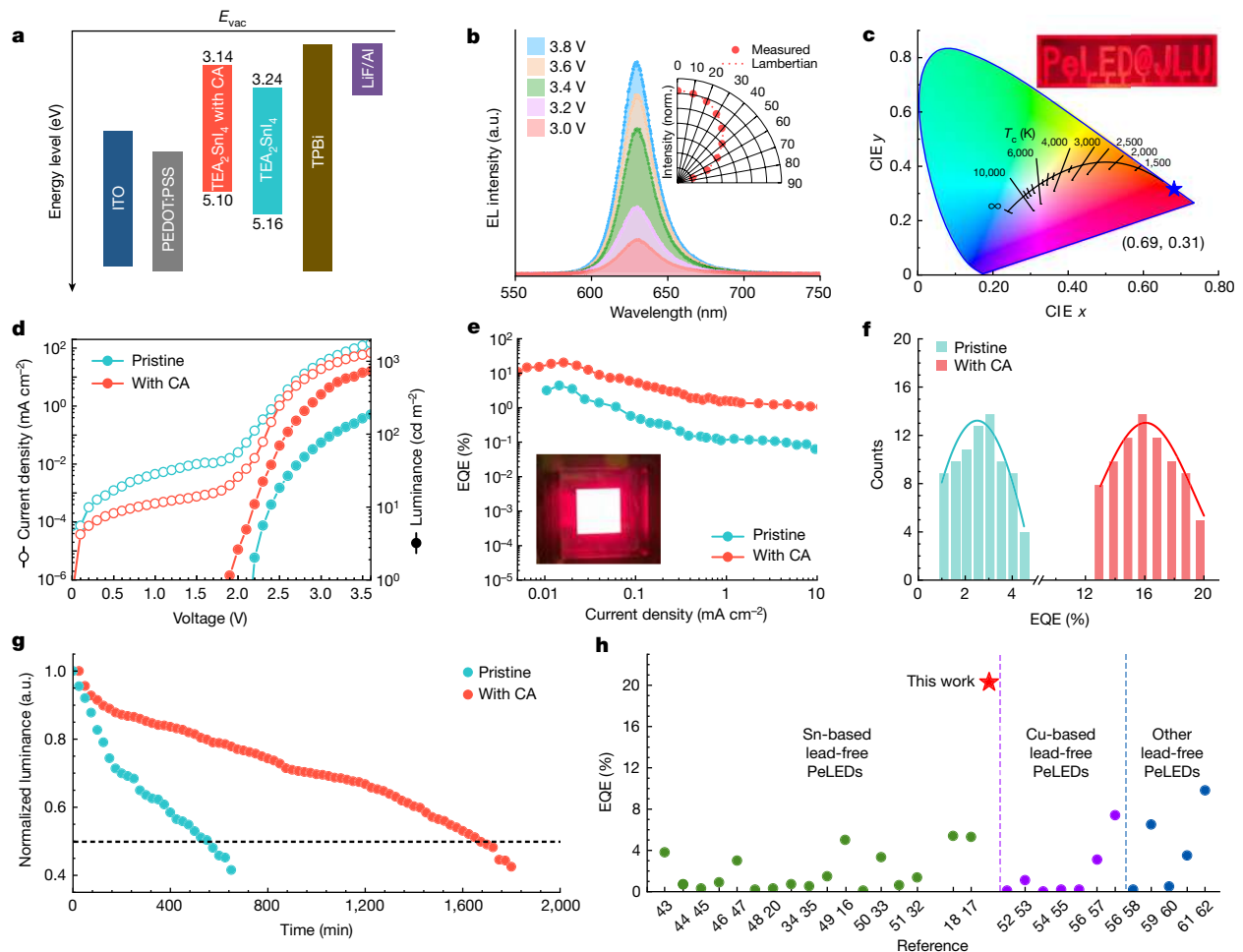


Fig. 4 | Device characterization. **a**, Energy-level diagram of the devices used in this work. **b**, Electroluminescence (EL) spectra of one target device with a constant peak emission wavelength of 630 nm under different voltages. Inset, an angle-dependent EL intensity measurement. **c**, Commission Internationale de L'Eclairage (CIE) colour space plot of one target device. Inset, photograph of a lead-free PeLED with the pattern 'PeLED@JLU'. **d**, J - V - L curves of the devices with and without CA. **e**, EQE- J curves of the devices with and without CA. Inset,

photograph of a working device (effective area: $1.5\text{ cm} \times 1.5\text{ cm}$). **f**, Histograms of peak EQEs measured from 80 devices in one batch for the Sn-PeLEDs with and without CA. **g**, Operational stability results of the devices with and without CA. The horizontal dashed line indicates half of the initial luminance. **h**, A comparison of the EQEs between our work and the previously reported results based on lead-free PeLEDs (Extended Data Table 1)^{16–18, 20, 32–35, 43–62}. a.u., arbitrary units.

LED performance

We then fabricated the Sn-PeLEDs with a conventional structure (Fig. 4a). The target Sn-PeLED showed electroluminescent spectra centred at about 630 nm under different voltages (Fig. 4b), and the luminance distribution is consistent with a Lambertian profile. The corresponding Commission Internationale de L'Eclairage (CIE) colour coordinates are (0.69, 0.31) (Fig. 4c), demonstrating a high colour-purity red emission. Compared with the reference device, the target Sn-PeLED had a narrower FWHM (24.9 nm) and showed stable steady-state electroluminescence output over 200 s (Supplementary Fig. 12), indicating greater potential in the field of pure-red lighting and displays. Figure 4d shows the current density–voltage–luminance (J – V – L) curves of the representative Sn-PeLEDs. The target devices attained a maximum EQE of 20.29%, which is considerably higher than that of the control Sn-PeLEDs (peak EQE of 4.37%) (Fig. 4e and Extended Data Fig. 8). A statistical distribution of EQEs of the Sn-PeLEDs is shown in Fig. 4f. The average EQE of the target Sn-PeLEDs was 16.28%, which is about sevenfold higher than that of the reference devices (2.6%). Noticeably, the turn-on voltage of the target device was 0.3 V lower than that of the pristine device, which is consistent with the enhanced luminance and EQE. These results demonstrated a reduction of non-radiative recombination in the target Sn-PeLEDs.

Moreover, ultraviolet photoelectron spectroscopy measurements showed that the target Sn perovskite layer had better band alignment with both electron- and hole-transporting layers, favouring charge injection and transport, which was further validated by the space-charge-limited current (SCLC) measurements (Supplementary Figs. 13 and 14). Operational stability tests were further conducted for the Sn-PeLEDs at a constant current density (initial luminance was 30 cd m^{-2} in an N_2 -filled glovebox). The target device demonstrated more than threefold longer operating half-life time (T_{50}) than that of the reference (27.6 h versus 9.1 h) (Fig. 4g), which is one of the best T_{50} results among lead-free PeLEDs. To highlight our work, we summarized the EQEs of lead-free PeLEDs reported so far (Fig. 4h and Extended Data Table 1). The champion EQE achieved is fully comparable to those of lead-based PeLEDs. We attribute the remarkable optoelectronic performance and operational stability of the lead-free PeLEDs to reduced defect density and halide ion migration, enhanced exciton binding energy and suppressed non-radiative recombination. Furthermore, the applicability of the CA tautomer-based mechanism is successfully extended to other two- and three-dimensional Sn-perovskites-based PeLEDs and the uniqueness of the proposed strategy is also demonstrated through structurally similar molecules with CA but not isomers (Extended Data Fig. 9, Supplementary Figs. 15–19 and Supplementary Table 4).

In summary, the existing performance barrier of lead-free PeLEDs was overcome by integrating CA into two-dimensional TEA_2SnI_4 and allowed us to achieve an EQE of more than 20%. The polyfunctional character of CA led to the formation of a well-oriented and highly stable tautomeric CA complex that enables strong chemical coordination to Sn(II) with beneficial effects on crystallographic orientation and shelf stability of the Sn perovskite films yielding improved radiative recombination. Notably, the cooperative coordination-induced electron localization of Sn(II) using CA di- or trimeric surface complex is key for stabilizing Sn(II). Beyond solid-state electroluminescence, this fundamental progress could be broadly used in many lead-free perovskite semiconductors applications.

Online content

Any methods, additional references, Nature Portfolio reporting summaries, source data, extended data, supplementary information, acknowledgements, peer review information; details of author contributions and competing interests; and statements of data and code availability are available at <https://doi.org/10.1038/s41586-023-06514-6>.

1. Kim, J. S. et al. Ultra-bright, efficient and stable perovskite light-emitting diodes. *Nature* **611**, 688–694 (2022).
2. Jiang, Y. et al. Synthesis-on-substrate of quantum dot solids. *Nature* **612**, 679–684 (2022).
3. Cao, Y. et al. Perovskite light-emitting diodes based on spontaneously formed submicrometre-scale structures. *Nature* **562**, 249–253 (2018).
4. Lei, Y. et al. Perovskite superlattices with efficient carrier dynamics. *Nature* **608**, 317–323 (2022).
5. Luo, J. et al. Efficient and stable emission of warm-white light from lead-free halide double perovskites. *Nature* **563**, 541–545 (2018).
6. Ma, D. et al. Distribution control enables efficient reduced-dimensional perovskite LEDs. *Nature* **599**, 594–598 (2021).
7. Lin, K. et al. Perovskite light-emitting diodes with external quantum efficiency exceeding 20 per cent. *Nature* **562**, 245–248 (2018).
8. Hassan, Y. et al. Ligand-engineered bandgap stability in mixed-halide perovskite LEDs. *Nature* **591**, 72–77 (2021).
9. Chiba, T. et al. Anion-exchange red perovskite quantum dots with ammonium iodine salts for highly efficient light-emitting devices. *Nat. Photon.* **12**, 681–687 (2018).
10. Jeong, J. et al. Pseudo-halide anion engineering for $\alpha\text{-FAPbI}_3$ perovskite solar cells. *Nature* **592**, 381–385 (2021).
11. Guo, B. et al. Ultrastable near-infrared perovskite light-emitting diodes. *Nat. Photon.* **16**, 637–643 (2022).
12. Kim, Y.-H. et al. Comprehensive defect suppression in perovskite nanocrystals for high-efficiency light-emitting diodes. *Nat. Photon.* **15**, 148–155 (2021).
13. Zhou, J. et al. Chemo-thermal surface dedoping for high-performance tin perovskite solar cells. *Mater.* **5**, 683–693 (2022).
14. Jiang, X. et al. One-step synthesis of $\text{SnI}_2(\text{DMSO})_x$ adducts for high-performance tin perovskite solar cells. *J. Am. Chem. Soc.* **143**, 10970–10976 (2021).
15. Yu, B.-B. et al. Heterogeneous 2D/3D tin-halides perovskite solar cells with certified conversion efficiency breaking 14%. *Adv. Mater.* **33**, 2102055 (2021).
16. Yuan, F. et al. Color-pure red light-emitting diodes based on two-dimensional lead-free perovskites. *Sci. Adv.* **6**, eabb0253 (2020).
17. Zhang, F. et al. Vapor-assisted in situ recrystallization for efficient tin-based perovskite light-emitting diodes. *Adv. Mater.* **34**, 2203180 (2022).
18. Lu, J. et al. Dendritic CsSnI_3 for efficient and flexible near-infrared perovskite light-emitting diodes. *Adv. Mater.* **33**, 2104414 (2021).
19. Heo, J.-M. et al. Bright lead-free inorganic CsSnBr_3 perovskite light-emitting diodes. *ACS Energy Lett.* **7**, 2807–2815 (2022).
20. Liang, H. et al. High color purity lead-free perovskite light-emitting diodes via Sn stabilization. *Adv. Sci.* **7**, 1903213 (2020).
21. Chen, M.-Y. et al. Strongly coupled tin-halide perovskites to modulate light emission: tunable 550–640 nm light emission (FWHM 36–80 nm) with a quantum yield of up to 6.4%. *Adv. Mater.* **30**, 1706592 (2018).
22. Cametti, G., Nagashima, M. & Churakov, S. V. Role of lone-pair electron localization in temperature-induced phase transitions in mimetite. *Acta Cryst. Eng. Mater.* **78**, 618–626 (2022).
23. Ye, T. et al. Localized electron density engineering for stabilized B-γ CsSnI_3 -based perovskite solar cells with efficiencies >10%. *ACS Energy Lett.* **6**, 1480–1489 (2021).
24. Pérez-Manríquez, L., Cabrera, A., Sansores, L. E. & Salcedo, R. Aromaticity in cyanuric acid. *J. Mol. Model.* **17**, 1311–1315 (2011).
25. Prabhaharan, M., Prabakaran, A. R., Srinivasan, S. & Gunasekaran, S. Density functional theory studies on molecular structure, vibrational spectra and electronic properties of cyanuric acid. *Spectrochim. Acta A Mol. Biomol. Spectrosc.* **138**, 711–722 (2015).
26. Zhang, J. et al. Understanding steric-charge-dependence of conjugated passivators on $\pi\text{-Pb}^{2+}$ bond strength for efficient all-inorganic perovskite solar cells. *Chem. Eng. J.* **431**, 134230 (2022).
27. Pedireddi, V., & Belhekar, D. Investigation of some layered structures of cyanuric acid. *Tetrahedron* **58**, 2937–2941 (2002).
28. Falvello, L., Pascual, I., Tomás, M. & Urriolabeitia, E. P. The cyanurate ribbon in structural coordination chemistry: an aggregate structure that persists across different coordination environments and structural types. *J. Am. Chem. Soc.* **119**, 11894–11902 (1997).
29. Zhang, Q. et al. Stable lead-free tin halide perovskites with operational stability >1200 h by suppressing tin(II) oxidation. *Angew. Chem. Int. Ed.* **61**, e202205463 (2022).
30. Zai, H. et al. Sandwiched electrode buffer for efficient and stable perovskite solar cells with dual back surface fields. *Joule* **5**, 2148–2163 (2021).
31. Liu, J. et al. Efficient and stable perovskite-silicon tandem solar cells through contact displacement by MgF_x . *Science* **377**, 302–306 (2022).
32. Jia, H. et al. Biuret induced tin-anchoring and crystallization-regulating for efficient lead-free tin halide perovskite light-emitting diodes. *Small* **18**, 2200036 (2022).
33. Wang, K. et al. Lead-free organic-perovskite hybrid quantum wells for highly stable light-emitting diodes. *ACS Nano* **15**, 6316–6325 (2021).
34. Gao, C. et al. Multifunctional naphthal sulfonic salt incorporated in lead-free 2D tin halide perovskite for red light-emitting diodes. *ACS Photonics* **7**, 1915–1922 (2020).
35. Liao, Y., Shang, Y., Wei, Q., Wang, H. & Ning, Z. Two-dimensional tin perovskite nanoplate for pure red light-emitting diodes. *J. Phys. D Appl. Phys.* **53**, 414005 (2020).
36. Ma, J.-Y., Ding, J., Yan, H.-J., Wang, D. & Hu, J.-S. Temperature-dependent local electrical properties of organic-inorganic halide perovskites: in situ KPFM and c-AFM investigation. *ACS Appl. Mater. Interfaces* **11**, 21627–21633 (2019).
37. Ren, Z. et al. Simultaneous low-order phase suppression and defect passivation for efficient and stable blue light-emitting diodes. *ACS Energy Lett.* **5**, 2569–2579 (2020).
38. Su, Y. et al. Acetic acid-assisted synergistic modulation of crystallization kinetics and inhibition of Sn^{2+} oxidation in tin-based perovskite solar cells. *Adv. Funct. Mater.* **32**, 2109631 (2022).
39. Lin, J. T. et al. Superior stability and emission quantum yield ($23\% \pm 3\%$) of single-layer 2D tin perovskite TEA_2SnI_4 via thiocyanate passivation. *Small* **16**, 2000903 (2020).
40. Zou, W. et al. Minimising efficiency roll-off in high-brightness perovskite light-emitting diodes. *Nat. Commun.* **9**, 608 (2018).
41. Luo, Y. et al. A multifunctional ionic liquid additive enabling stable and efficient perovskite light-emitting diodes. *Small* **18**, 2200498 (2022).
42. Zhang, T. et al. Regulation of the luminescence mechanism of two-dimensional tin halide perovskites. *Nat. Commun.* **13**, 60 (2022).
43. Hong, W.-L. et al. Efficient low-temperature solution-processed lead-free perovskite infrared light-emitting diodes. *Adv. Mater.* **28**, 8029–8036 (2016).
44. Lai, M. L. et al. Tunable near-infrared luminescence in tin halide perovskite devices. *J. Phys. Chem. Lett.* **7**, 2653–2658 (2016).
45. Yuan, F. et al. All-inorganic hetero-structured cesium tin halide perovskite light-emitting diodes with current density over 900 A cm^{-2} and its amplified spontaneous emission behaviors. *Phys. Status Solidi Rapid Res. Lett.* **12**, 1800090 (2018).
46. Qiu, W. et al. Mixed lead-tin halide perovskites for efficient and wavelength-tunable near-infrared light-emitting diodes. *Adv. Mater.* **31**, 1806105 (2019).
47. Wang, Y. et al. Tin-based multiple quantum well perovskites for light-emitting diodes with improved stability. *J. Phys. Chem. Lett.* **10**, 453–459 (2019).
48. Mu, H., Hu, F., Wang, R., Jia, J. & Xiao, S. Effects of in-situ annealing on the electroluminescence performance of the Sn-based perovskite light-emitting diodes prepared by thermal evaporation. *J. Lumin.* **226**, 117493 (2020).
49. Wang, X., Liu, L., Qian, Z., Gao, C. & Liang, H. Eu^{2+} ions as an antioxidant additive for Sn-based perovskite light-emitting diodes. *J. Mater. Chem. C* **9**, 12079–12085 (2021).
50. Zhang, X. et al. Bright orange electroluminescence from lead-free two-dimensional perovskites. *ACS Energy Lett.* **4**, 242–248 (2019).
51. Wang, Z. et al. Efficient two-dimensional tin halide perovskite light-emitting diodes via a spacer cation substitution strategy. *J. Phys. Chem. Lett.* **11**, 1120–1127 (2020).
52. Liu, X. et al. Vacuum dual-source thermal-deposited lead-free Cs_2CuI_3 films with high photoluminescence quantum yield for deep-blue light-emitting diodes. *ACS Appl. Mater. Interfaces* **12**, 52967–52975 (2020).
53. Wang, L. et al. Colloidal synthesis of ternary copper halide nanocrystals for high-efficiency deep-blue light-emitting diodes with a half-lifetime above 100 h. *Nano Lett.* **20**, 3568–3576 (2020).
54. Liu, N. et al. Light-emitting diodes based on all-inorganic copper halide perovskite with self-trapped excitons. *J. Semicond.* **41**, 052204 (2020).
55. Ma, Z. et al. Stable yellow light-emitting devices based on ternary copper halides with broadband emissive self-trapped excitons. *ACS Nano* **14**, 4475–4486 (2020).
56. Seo, G. et al. Lead-free halide light-emitting diodes with external quantum efficiency exceeding 7% using host-dopant strategy. *ACS Energy Lett.* **6**, 2584–2593 (2021).
57. Chen, H. et al. Efficient and bright warm-white electroluminescence from lead-free metal halides. *Nat. Commun.* **12**, 1421 (2021).
58. Ma, Z. et al. Electrically-driven violet light-emitting devices based on highly stable lead-free perovskite $\text{Cs}_3\text{Sb}_2\text{Br}_9$ quantum dots. *ACS Energy Lett.* **5**, 385–394 (2019).
59. Luo, J. et al. Efficient blue light emitting diodes based on europium halide perovskites. *Adv. Mater.* **33**, 2101903 (2021).
60. Wang, L. et al. Exploration of nontoxic Cs_3CeBr_6 for violet light-emitting diodes. *ACS Energy Lett.* **6**, 4245–4254 (2021).
61. Guo, Q. et al. Spectra stable deep-blue light-emitting diodes based on cryolite-like cerium(III) halides with nanosecond d-f emission. *Sci. Adv.* **8**, eabq2148 (2022).
62. Yan, S. et al. Synthesis of OD manganese-based organic-inorganic hybrid perovskite and its application in lead-free red light-emitting diode. *Adv. Funct. Mater.* **31**, 2100855 (2021).

Publisher's note Springer Nature remains neutral with regard to jurisdictional claims in published maps and institutional affiliations.

Springer Nature or its licensor (e.g. a society or other partner) holds exclusive rights to this article under a publishing agreement with the author(s) or other rightsholder(s); author self-archiving of the accepted manuscript version of this article is solely governed by the terms of such publishing agreement and applicable law.

© The Author(s), under exclusive licence to Springer Nature Limited 2023, corrected publication 2024

Methods

Materials

Tin (II) iodide (SnI_2), tin (II) bromide (SnBr_2), caesium bromide (CsBr) and caesium iodide (CsI) were purchased from Advanced Electron Technology. Toluene was purchased from Sigma Aldrich, silver (Ag) from Alfa Aesar, aluminium (Al) from Alfa Aesar, tin powder from Alfa Aesar, lithium fluoride (LiF) from Aladdin and rubidium iodide (RbI) from Sigma Aldrich. Glasses coated with patterned indium tin oxide (ITO) (approximately $15\ \Omega\ \text{sq}^{-1}$) were purchased from Jinge-Solar Tech. 2-Thiopheneethylamine iodide and poly(3,4-ethylenedioxythiophene)/poly(styrenesulphonate) (PEDOT:PSS) were purchased from Heraeus Clevios Al 4083, and phenylethyl ammonium iodide (PEAI) and 2,2',2''-benzene-1,3,5-triyltris(1-phenyl-1H-benzimidazole) (TPBi) were purchased from Xi'an Polymer Light Technology. Phloroglucinol, melamine, molybdenum trioxide (MoO_3), *N,N*-dimethylformamide (DMF), dimethyl sulphoxide (DMSO) and CA were purchased from Innochem. Polymethyl methacrylate (PMMA) was purchased from Sigma Aldrich and KBr from Aladdin. All these materials were used without further purification.

Preparation of TEA_2SnI_4 perovskite films

For Sn perovskite precursor solution (0.2 M), 2-thiopheneethylamine iodide and SnI_2 with a molar ratio of 2.2:1 were dissolved in anhydrous DMF:DMSO (4:1 v/v) solution, and RbI (6 mg ml^{-1}) and tin powder (50 mg ml^{-1}) were added. The precursor solution was stirred in an N_2 -filled glovebox (H_2O and O_2 , <0.01 ppm) overnight at 50 °C and then filtered with a 0.22-μm polytetrafluoroethylene (PTFE) filter before use. The Sn perovskite films were spin-coated by a one-step process, 50-μl perovskite precursor (concentrations of 0%, 2%, 5% and 8% CA) was dropped onto the PEDOT:PSS substrates at 5,000 rpm for 55 s, and then 200 μl anhydrous toluene was dropped onto the substrate at 10 s after spin-coating. Finally, the obtained perovskite thin films were annealed at 100 °C for 10 min inside a glovebox. The corresponding films are denoted as pristine, with 2% CA, with 5% CA, and with 8% CA, respectively. In this text, with 5% CA is abbreviated as 'with CA'. Also, the perovskite nanoplates were prepared using a previously described method³⁹. The preparation process of PEA_2SnI_4 perovskite films is the same as that of TEA_2SnI_4 . For CsSnBr_3 and $\text{CsSnBr}_{2.5}\text{J}_{0.5}$, stoichiometric ratios of $\text{CsBr}:\text{SnBr}_2 = 1:1$ and $\text{CsBr}:\text{CsI}:\text{SnBr}_2 = 0.5:0.5:1$ were dissolved in DMSO with a concentration of 0.2 M, and CA was added.

Device fabrication

The ITO-coated glass substrates were ultrasonically cleaned for 20 min with detergent, deionized water, acetone and isopropyl alcohol. Next, the cleaned ITO-coated glass substrates were treated with ultraviolet (UV) light and ozone for 20 min. Modified PEDOT:PSS solution was prepared by mixing PEDOT:PSS solution with deionized water with a volume ratio of 7:3. Then, the PEDOT:PSS solution was spin-coated onto the treated ITO substrate at 4,000 rpm for 30 s and then the substrates were annealed in air at 150 °C for 20 min. After that the substrates were transferred to an N_2 -filled glovebox for 20-min annealing (150 °C) again. After spin-coating the Sn perovskite films as described above, the substrates were transferred to a vacuum thermal evaporator. Finally, 30 nm TPBi, 1 nm LiF and 100 nm Al electrode were deposited in sequence, under a high vacuum of less than 5×10^{-4} Pa. The effective area was defined using masks as 0.06 cm^2 .

Characterizations

Steady-state PL (Omni-λ 300 Monochromator/Spectrometer, Zolix) and TRPL (Horiba DeltaPro fluorescence lifetime system) measurements were performed with Sn perovskite films spin-coated on quartz substrates. The TRPL curves were fitted with biexponential equations:

$$I = A + B_1 e^{-t/\tau_1} + B_2 e^{-t/\tau_2} \quad (1)$$

where I is the normalized PL intensity, A , B_1 and B_2 are the decay amplitudes and $A + B_1 + B_2 = 1$. τ_1 and τ_2 correspond to the lifetime constants of fast and slow components, respectively. τ_{average} is given by the equation below:

$$\tau_{\text{average}} = B_1 \tau_1 + B_2 \tau_2 \quad (2)$$

For temperature-dependent PL measurements, Sn perovskite films prepared on quartz substrates were mounted in a cryostat (Janis ST-100) and cooled by liquid nitrogen. The samples were excited by a continuous-wave laser at an excitation wavelength of 400 nm (power density of $2\ \mu\text{J}\ \text{cm}^{-2}$ and at 20 K intervals). XRD results were collected from the Rigaku Smart Lab X-ray diffractometer with Cu K α radiation ($\lambda = 1.54050\ \text{\AA}$). The GIWAXS was performed at the BL17B1 and BL19U2 beamline of SSRF using an X-ray energy of 10 keV. Two-dimensional patterns of Sn perovskite films on silicon-wafer substrates were acquired by a PLATUS 2M detector mounted vertically at a distance of about 240 mm from the sample with a grazing incidence angle of around 0.2–0.4° and an exposure time of 20 s. Electrochemical impedance spectroscopy experiments of the Sn-PeLED devices were carried out with an electrochemical workstation (CHI660C, CH Instruments). All Sn-PeLED devices were measured in an N_2 -filled glovebox using Keithley 2400 and Konica Minolta CS-200. Electroluminescence characteristics were recorded with a Flame spectrometer and an integrating sphere (Ocean Optic). The sweeping bias range is from 0 V to 10 V with a bias step of 100 mV and a delay time of 1 s. A schematic of the measurement system for our PeLEDs is shown in Supplementary Fig. 12h. The light distribution was measured using a Konica Minolta CS-200 detector, coordinating with various angles from 0° to 90°. Morphology and energy dispersive X-ray spectroscopy of the Sn perovskite films were characterized by scanning electron microscope (Hitachi S-4800). Atomic force microscope measurements were performed using a Bruker Nano ICON2-SYS microscope (Germany). Kelvin probe force microscopy potential and topographic mappings were obtained using a Digital Instruments Multimode atomic force microscope (Veeco Metrology Group), and the used Sn perovskite films were deposited on the ITO/PEDOT:PSS substrate. The optical properties of the Sn perovskite films were measured using ultraviolet light-visible (UV-vis) absorption spectroscopy (Shimadzu UV-vis-NIR spectrometer (UV-2600i)). Transient-absorption spectroscopy measurements were performed using a commercial set-up (Helios, Ultrafast Systems). The wavelength and the energy density of the pump pulse were 400 nm and $8\ \mu\text{J}\ \text{cm}^{-2}$, respectively. The perovskite films for transient-absorption characterization were fabricated on quartz substrates, spin-coating a layer of PMMA with a concentration of 20 mg ml^{-1} on the perovskite surface. XPS and ultraviolet photoelectron spectroscopy spectra were obtained with Hitachi Regulus 8100. The excitation-intensity-dependent PLQYs were measured by a custom instrument combining a 405-nm laser, spectrometer and integrating sphere. NMR, ^1H NMR and ^{13}C NMR spectra were recorded using Bruker AVIII 500MHz FT-NMR. FTIR spectroscopy was tested with Thermo Scientific Nicolet iS10 Instrument, the powder scraped from the perovskite films was mixed with dry KBr powder and ground directly, and pressure was applied to press the powder into a transparent sheet for testing. The electrostatic potentials (ESPs) were calculated using Gaussview software using a self-consistent field-density matrix. The TEM measurements were performed using a JEM-2200FSF microscope.

Defect density and carrier mobility calculations

The defect density can be deduced from the onset voltage of the trap-filled limit region (V_{TFL}), as shown in equation (3). The carrier mobility of the Sn perovskite films was obtained by the SCLC method using the Mott–Gurney law equation (4):

$$N_t = 2\epsilon_0\epsilon_r V_{\text{TFL}}/qL^2 \quad (3)$$

$$J = 9/8\mu\epsilon_0\epsilon_r V_{TFL^2}/L^3 \quad (4)$$

where L is the thickness of perovskite film, ϵ_r is the relative dielectric constant, ϵ_0 is the vacuum permittivity, q is the charge constant and μ is the carrier mobility. The hole-only device with an architecture of ITO/PEDOT:PSS/perovskite/MoO₃(30 nm)/Ag(100 nm) was used. The electron-only device with a structure of ITO/TPBi(30 nm)/perovskite/TPBi(30 nm)/LiF(3 nm)/Ag(100 nm) was used.

Stability measurement

The stability of the LED was measured in an N₂-filled glovebox at room temperature without encapsulation under dark conditions. The devices were driven by a Keithley 2400 source meter at a constant current, and the luminance was measured using a Konica Minolta CS-200 with an initial luminance of 30 cd m⁻².

Arrhenius equation

$$I(T) = I_0/(1 + Ae^{-E_b/k_B T}) \quad (5)$$

where I_0 is the PL intensity at 0 K, k_B is the Boltzmann constant and E_b is the exciton binding energy.

System model

The structure of TEA₂SnI₄ was initially built by combining the inorganic framework of FA₂SnI₄ (FA is formamidinium) with the TEA cations (instead of FA). The distance between the Pb–I layers was initially set to 15.45 Å, as obtained from the XRD measurements. To model the surface, we built a slab containing two inorganic layers (Extended Data Fig. 2) and a vacuum space of 17 Å. For the AIMD simulations, this model was expanded to a 4 × 3 × 1 supercell.

Static DFT calculations

The structural and electronic properties of Sn perovskite surfaces have been investigated by first-principles calculations based on density functional theory (DFT) as implemented in the Vienna ab initio simulation package (VASP)^{63,64}. The standard frozen-core projector-augmented wave method was used to describe the interactions between the ions and electrons. Exchange-correlation effects were included using the generalized gradient approximation of the Perdew–Burke–Ernzerhof (PBE) functional⁶⁵. The kinetic energy cutoff was set at 400 eV for the plane-wave expansion. The Monkhorst–Pack k -point grid with a resolution of 0.2 Å⁻¹ was selected to sample the reciprocal space for the calculated systems⁶⁶. A vacuum space of 20 Å was set between the adjacent images to avoid any fictitious interactions. Dipole corrections (IDIPOL = 3) were employed to correct for the slab-to-slab dipole interactions along the surface normal direction. Grimme's dispersion correction scheme combined with Becke–Johnson damping was considered to correct for van der Waals interactions⁶⁷. The bottom layers were fixed at the bulk crystal geometry⁶⁸. The geometry optimizations were performed with a convergence criterion of 1.0×10^{-6} eV in energy and 0.005 eV Å⁻¹ in forces. Calculations of the capture coefficient calculation were based on the previous literature^{69,70}. Non-radiative recombination coefficient B , which is defined as $B = N_{\text{def}}A$, where N_{def} is the defect density from being obtained single carrier devices and A is the non-radiative recombination capture coefficient.

AIMD simulations

The Born–Oppenheimer AIMD (DFT-based) simulations with a mixed Gaussian and plane wave (GPW) basis as implemented in the CP2K package^{71–74} were performed to investigate the interaction between the molecules and the perovskite surface. The valence electrons were expanded in a double-ζ Gaussian basis set with polarization functions (DZVP)⁷⁵. The energy cutoff for the electron density expansion in the

GPW method was 400 Ry. The temperature was controlled by the velocity rescaling thermostat of a previous study⁷⁶ with a time constant of 0.5 fs. All AIMD simulations were performed at the Γ -point. For the three Sn-based perovskite surfaces (TEA₂SnI₄, PEA₂SnI₄ and CsSnI₃), the lattice parameters of the triclinic simulation box were allowed to relax for 2 ps in the isothermal–isobaric ensemble (NPT) with $P = 1$ atm. The systems were then equilibrated over 5 ps in the NVT ensemble using the supercell volume obtained by the NPT simulation reshaped in an orthorhombic box. All the slabs were considered Sn–I terminated on both sides. The final box sizes as well as the atomic compositions of each system were reported in Supplementary Table 5. For the adsorption of the CA trimer on TEA₂SnI₄, 25 ps of simulation runs were used to estimate interaction patterns between the molecules and the surface. The vibrational power spectra are computed as the Fourier transform of the autocorrelation function of the atomic velocities. Three CA concentrations (CA molecules relative to Sn species, 4.16%, 8.33% and 12.5%) and two different starting scenarios (pure keto and pure enol CA isomers) were considered in the simulations (Extended Data Fig. 2). Simulations show that pure keto isomer cannot be adsorbed stably on the Sn perovskite surface at any CA concentration. The final configurations of the CA trimer on the PEA₂SnI₄ and CsSnI₃ surfaces were considered stable after 10 ps of simulations run, when no conformational changes were further observed.

Data availability

The data that support the findings of this study are available from the corresponding authors.

63. Kresse, G. & Furthmüller, J. Efficiency of ab-initio total energy calculations for metals and semiconductors using a plane-wave basis set. *Comput. Mater. Sci.* **6**, 15–50 (1996).
64. Kresse, G., & Joubert, D. From ultrasoft pseudopotentials to the projector augmented-wave method. *Phys. Rev. B* **59**, 1758–1775 (1999).
65. Blöchl, P. E. Projector augmented-wave method. *Phys. Rev. B* **50**, 17953–17979 (1994).
66. Perdew, J. P., Burke, K. & Ernzerhof, M. Generalized Gradient Approximation Made Simple. *Phys. Rev. Lett.* **77**, 3865–3868 (1996).
67. Pack, J. D., & Monkhorst, H. J. “Special points for Brillouin-zone integrations”—a reply. *Phys. Rev. B* **16**, 1748–1749 (1977).
68. Grimme, S. et al. Semiempirical GGA-type density functional constructed with a long-range dispersion correction. *J. Comput. Chem.* **27**, 1787–1799 (2006).
69. Turiansky, M. E. et al. Nonrad: computing nonradiative capture coefficients from first principles. *Comput. Phys. Commun.* **267**, 108056 (2021).
70. Perdew, J. P. et al. Restoring the density-gradient expansion for exchange in solids and surfaces. *Phys. Rev. Lett.* **100**, 136406 (2008).
71. Alkauskas, A., Yan, Q., & van de Walle, First-principles theory of nonradiative carrier capture via multiphonon emission. *Phys. Rev. B* **90**, 075202 (2014).
72. Kresse, G., & Hafner, J. *Ab initio* molecular-dynamics simulation of the liquid-metal–amorphous-semiconductor transition in germanium. *Phys. Rev. B* **49**, 14251–14269 (1994).
73. Grimme, S., Antony, J., Ehrlich, S. & Krieg, H. A consistent and accurate *ab initio* parametrization of density functional dispersion correction (DFT-D) for the 94 elements H–Pu. *J. Chem. Phys.* **132**, 154104 (2010).
74. Tang, H. et al. Plasmonic hot electrons for sensing, photodetection, and solar energy applications: a perspective. *J. Chem. Phys.* **152**, 220901 (2020).
75. Fletcher, R. E., Ling, S. & Slater, B. Violations of Löwenstein's rule in zeolites. *Chem. Sci.* **8**, 7483–7491 (2017).
76. Bussi, G., Donadio, D. & Parrinello, M. Canonical sampling through velocity rescaling. *J. Chem. Phys.* **126**, 014101 (2007).

Acknowledgements This work was partly supported by the National Natural Science Foundation of China (grant nos. 51972137, 12175298 and 62174104), the Science and Technology Planning Project of Jilin Province (grant no. 20190201306JC) and the start-up funding of Jilin University. Y.Y. acknowledges the financial support from the Shanghai Municipal Commission for Science and Technology (no. 20ZR1464100). U.R. acknowledges the Swiss National Science Foundation (grant no. 200020-185092) for funding as well as computational resources from the Swiss National Computing Centre CSCS. M.G. acknowledges financial support from the European Union's Horizon 2020 research and innovation programme under grant agreement no. 881603. We thank the staff of beamlines BL17B1, BL19U1 and BL19U2 at SSRF for providing the beam time and the User Experiment Assist System of SSRF for their help. We thank M. Yao and J. Ning for discussions and G. Chen for TA measurements.

Author contributions H.L., X.Y., N.W. and M.G. supervised this project. N.W. conceived the idea. D.H. and J.W. fabricated and characterized the PeLED devices. D.H., J.W. and Z.Z. fabricated the perovskite films for experimental measurements. L.A., B.Z., H.J., I.M.-L., V.C.,

L.P. and S.M.Z. conducted the simulations under the guidance of U.R. J.Z. performed the film morphology measurements. J.D. and D.H. conducted XRD and temperature-dependent steady-state PL spectra measurements. Y.Y. and L.K. conducted the GIWAXS measurements. D.H., B.W. and Y.Y. analysed the results of GIWAXS and TA measurements. N.W., H.L., X.Y., Y.Y., D.H., J.W., Z.Z., I.M.-L., V.C., L.A., L.P., S.M.Z., U.R. and M.G. prepared and polished the paper. All authors discussed the results and commented on the paper.

Competing interests The authors declare no competing interests.

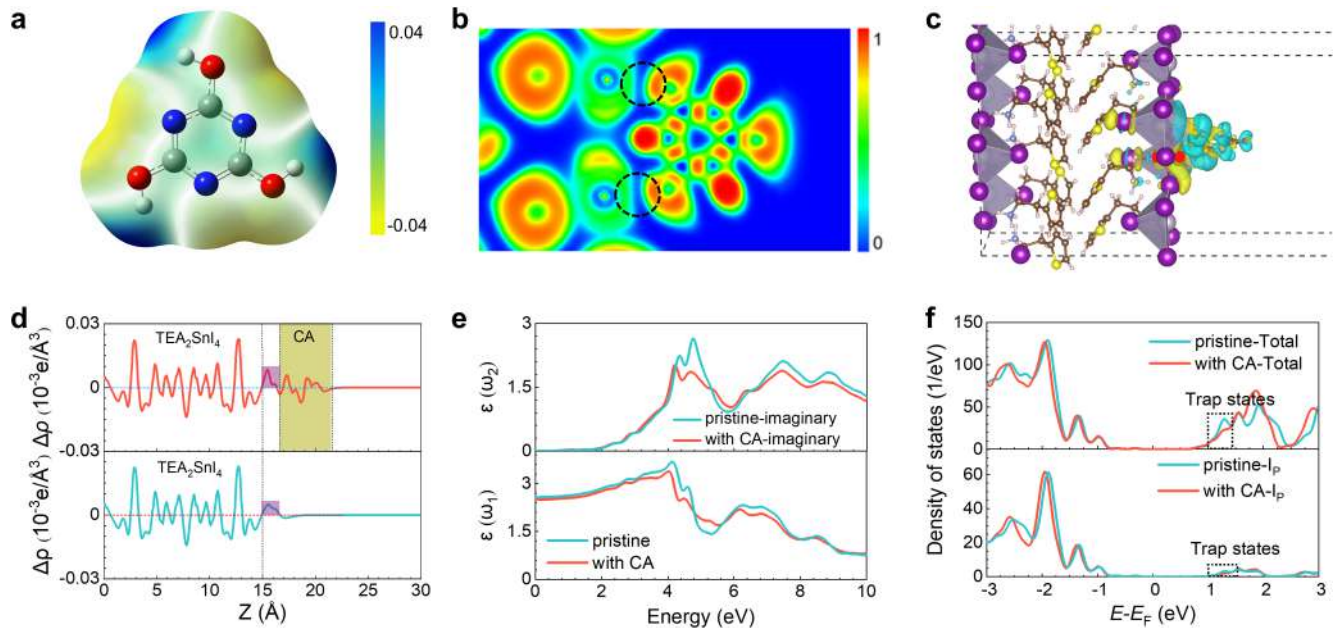
Additional information

Supplementary information The online version contains supplementary material available at <https://doi.org/10.1038/s41586-023-06514-6>.

Correspondence and requests for materials should be addressed to Haizhou Lu, Xuyong Yang, Michael Grätzel or Ning Wang.

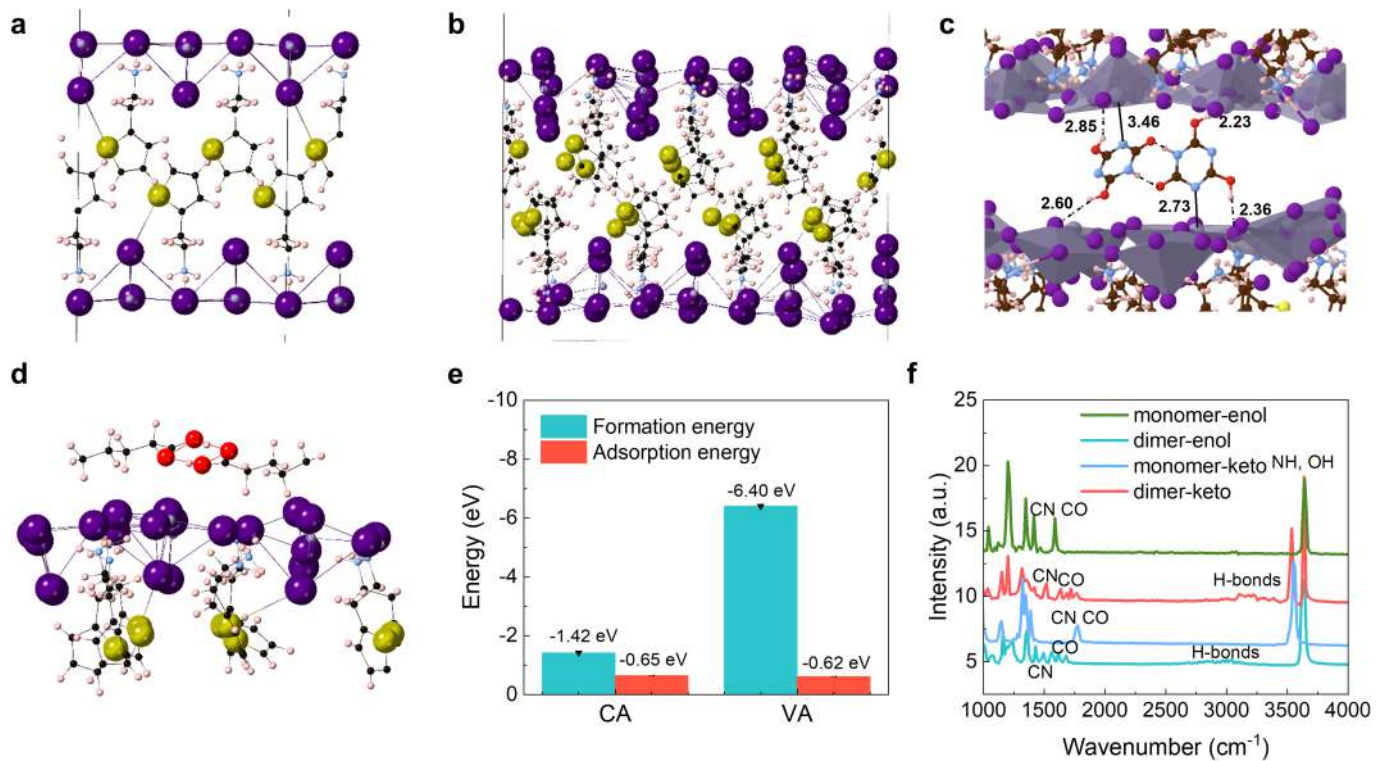
Peer review information *Nature* thanks Junghwan Kim and the other, anonymous, reviewer(s) for their contribution to the peer review of this work.

Reprints and permissions information is available at <http://www.nature.com/reprints>.



Extended Data Fig. 1 | Density functional theory study. **a**, Calculated electrostatic potential distribution for enol form of the CA molecule. **b**, Electron localization function image for the triketo CA-treated perovskite. **c**, Charge density difference between the tin perovskite and triketo CA. Obtained in systems with an iodide vacancy. **d**, Planar-averaged charge density difference

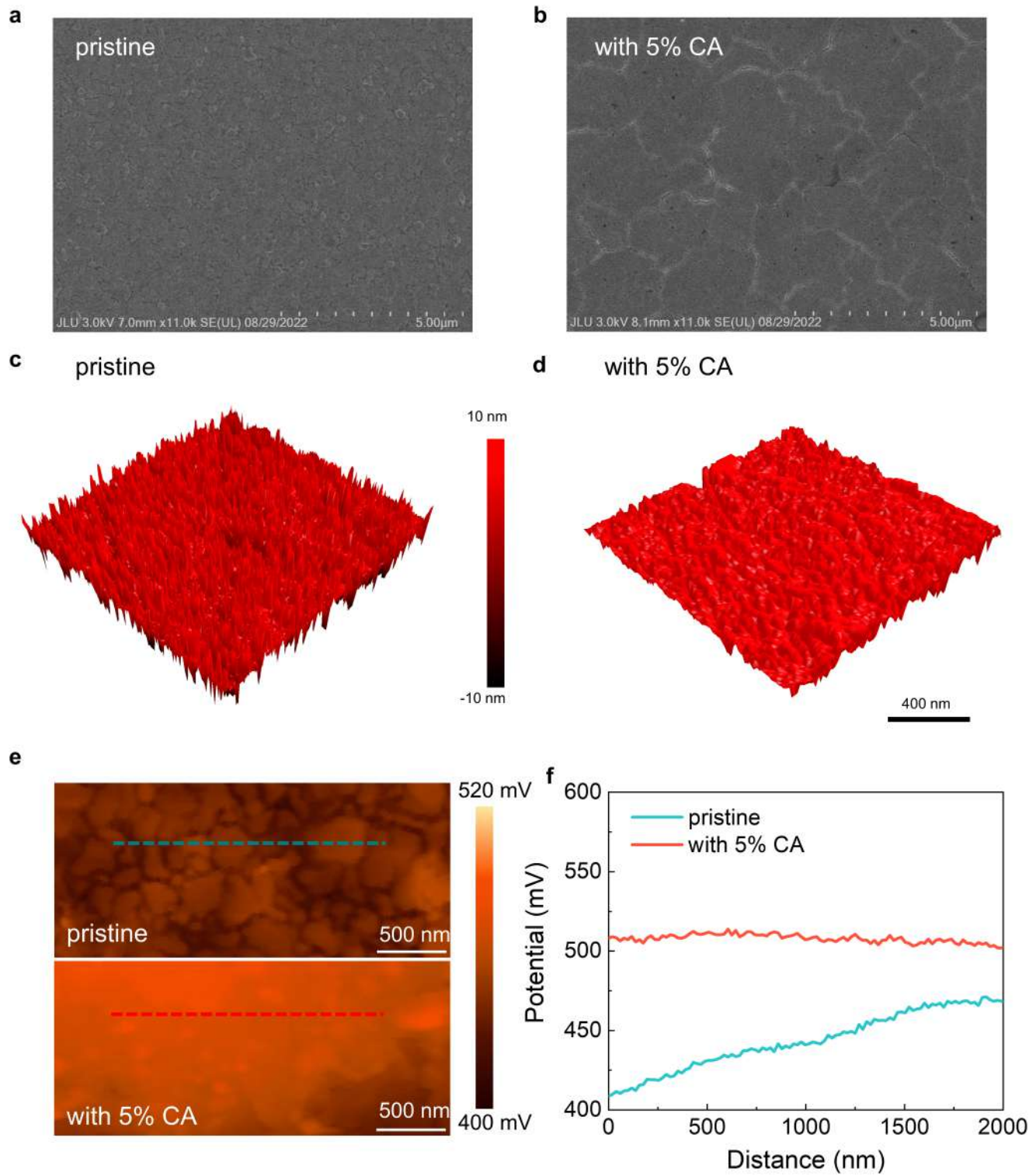
of the pristine and the Sn perovskite with CA. **e**, Dielectric coefficients of the Sn perovskites with and without CA along the Z -axis. **f**, Density of states for the pristine (blue) and the CA-treated perovskite (red) with a surface iodide vacancy.



Extended Data Fig. 2 | Configuration and FTIR studies. **a, b**, Built slab containing two inorganic layers (**a**) and a vacuum space of 17 Å. For the ab-initio molecular dynamics simulations, this model was expanded to a 4×3×1 supercell (**b**). Color code: Sn in grey, I in purple, S in yellow, C in black, H in pink, O in red, N in blue. **c**, AIMD snapshot of a stable dimer at a perovskite grain boundary. The distances are in Å. Color code: Sn in grey, I in purple, S in yellow, C in black, H in pink, O in red, N in blue. **d**, Valeric acid dimer on top of a pristine TEA_2SnI_4 surface. The protons are shared between two oxygens with distances of 1.0 Å and 1.6 Å. Valeric acid only contains one functional group - thus if the carboxylic acid group is used to form dimers, the molecule can no longer bind to the perovskite surface, as observed with ab initio MD simulations. **e**, Dimer formation energies (blue) and adsorption energies (red) for CA and valeric acid (VA). **f**, Vibrational power spectra of the CA keto and enol monomers and dimers in gas phase. The mixed enol-keto form can also explain the observed CO stretch in FTIR. This figure shows the vibrational power spectra of the gas

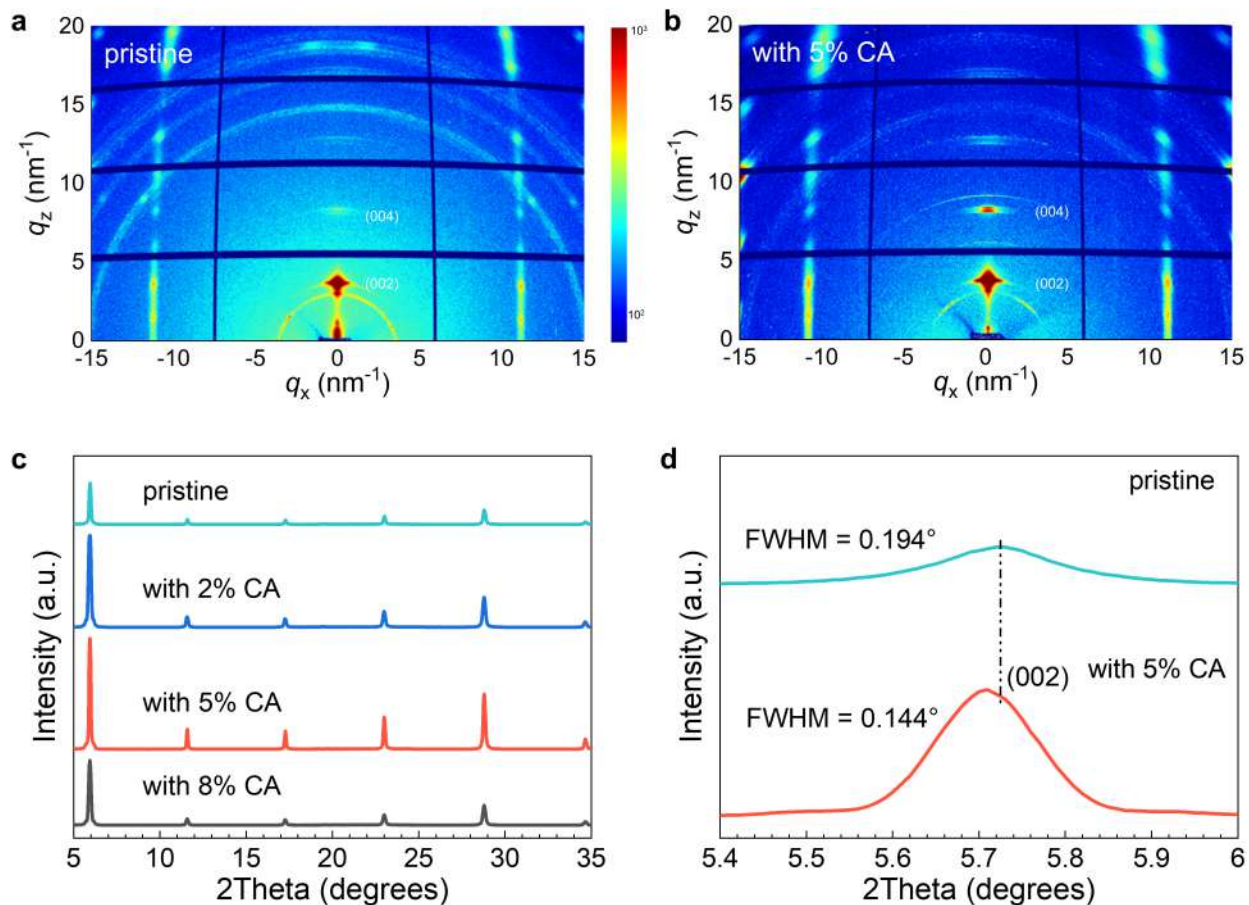
phase molecules of monomers and dimers of the pure keto and pure enol CA form. In the monomeric form, the CN and CO modes overlap at 1587 cm⁻¹ and 1775 cm⁻¹ for the enol and keto forms, respectively. Upon dimerization, these peaks split into three components with the CO contribution blue shifted compared to the CN one. From these results we can conclude that the experimental spectra contain contributions from mixed keto/enol dimers. Furthermore, Fig. 1 shows the computed vibrational power spectra of the most stable trimer configuration in vacuum and adsorbed on the perovskite surface. When the trimer is adsorbed on the surface, a blue shift of 25 cm⁻¹ and 15 cm⁻¹ is reported for CN and CO modes, respectively, in agreement with the experimental data. Another clear signature that CA adsorbs in the form of trimers and/or dimers is the peak around 3000–3300 cm⁻¹ due to OH and NH groups involved in H-bond interactions (CO-HNC); indeed, this kind of peaks are not present for monomers.

Article



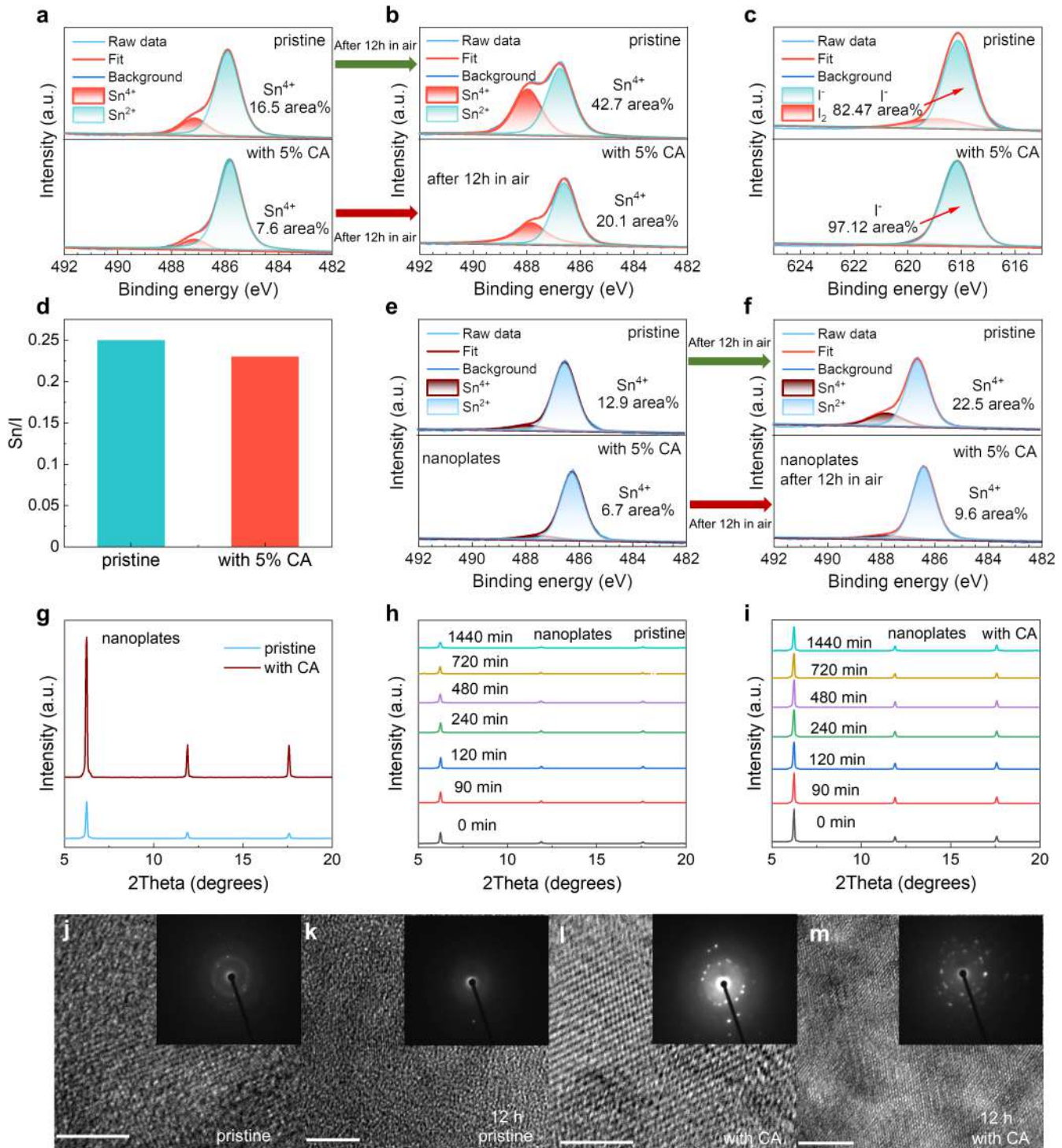
Extended Data Fig. 3 | Morphological characteristics. **a, b**, SEM images of the perovskite films without (**a**) and with 5% CA (**b**). **c, d**, AFM images of the pristine (**c**) and the 5% CA-treated sample (**d**). **e**, KPFM measurements for the

pristine and the CA-treated sample. **f**, Linear potential profiles for the pristine and the CA-treated sample.



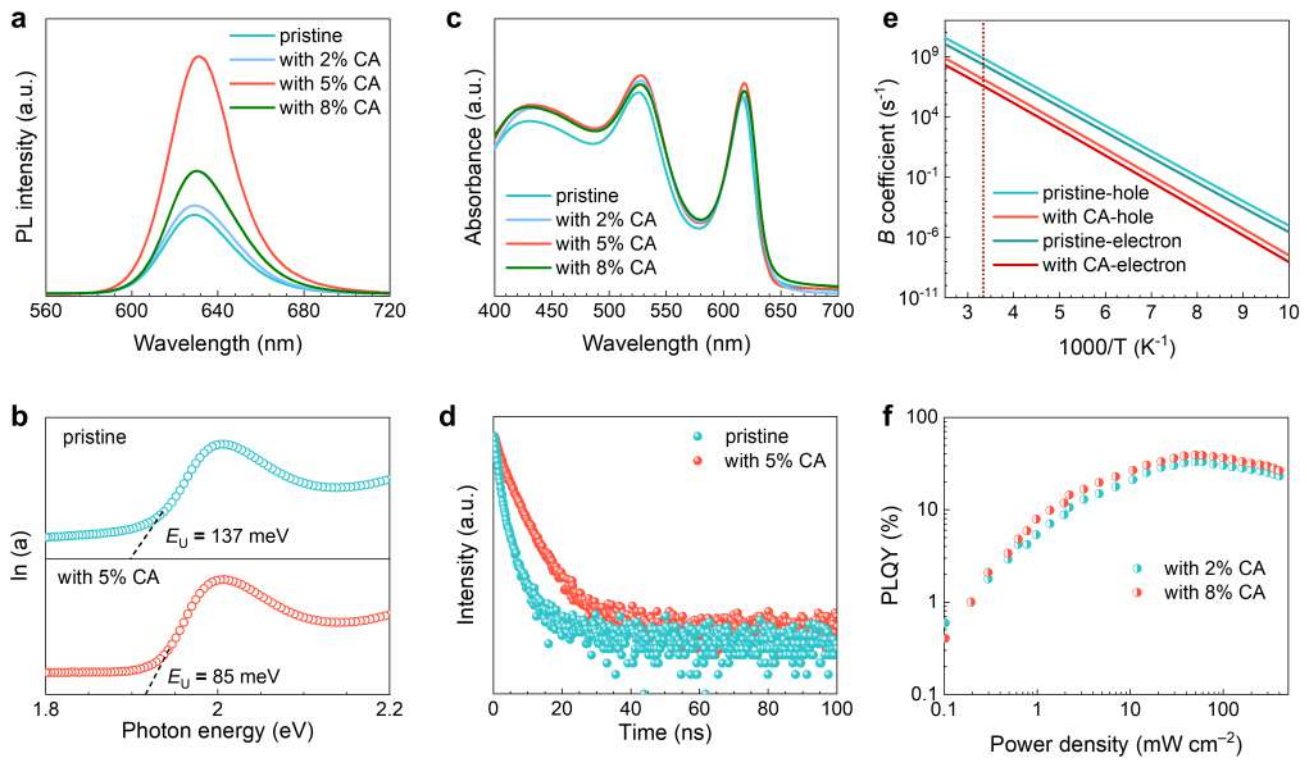
Extended Data Fig. 4 | Crystal structure of TEA₂SnI₄ films. **a, b**, GIWAXS images of TEA₂SnI₄ perovskite films without (a) and with 5% CA (b). **c**, XRD patterns of the pristine and the samples with 2%, 5% and 8% CA. **d**, Comparison of (002) peak for the samples with and without 5% CA.

Article



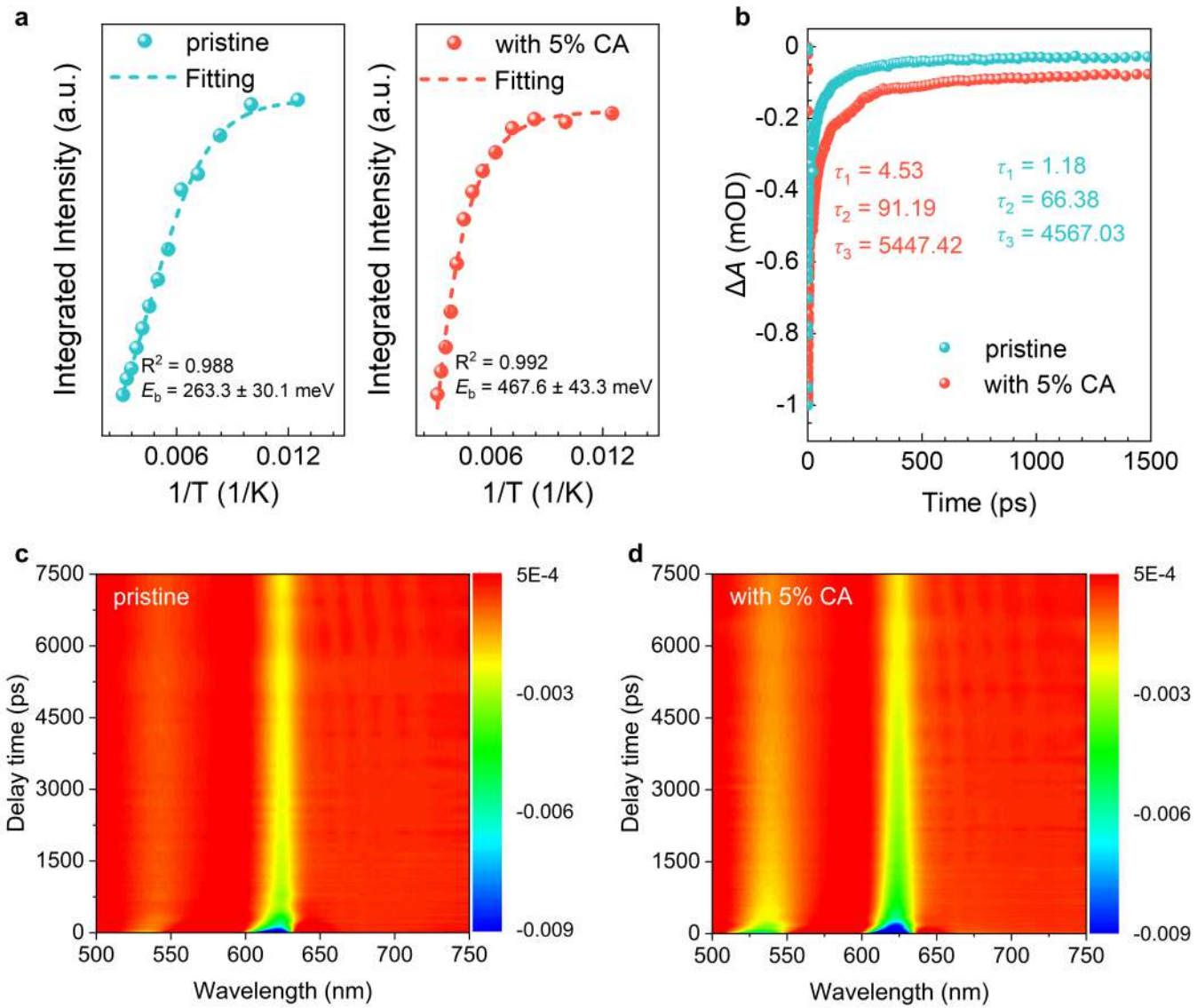
Extended Data Fig. 5 | XPS and air-stability analysis of TEA₂SnI₄ perovskites. **a**, XPS spectra of Sn 3d for the pristine and the CA-treated TEA₂SnI₄. **b**, XPS spectra of Sn 3d for the pristine and the CA-treated TEA₂SnI₄ stored in dry air for 12 h. **c**, XPS results of I 3d spectra for the tin perovskite films without and with 5% CA. **d**, Ratios of Sn versus I from the XPS spectra for the tin perovskite samples with and without CA. **e**, XPS spectra of Sn 3d for the pristine and the CA-treated TEA₂SnI₄ nanoplates. **f**, XPS spectra of Sn 3d for the pristine and the CA-treated TEA₂SnI₄ nanoplates stored in dry air for 12 h. **g**, XRD patterns of TEA₂SnI₄ nanoplates with and without CA. **h**, Time-dependent XRD patterns of TEA₂SnI₄ nanoplates without CA stored in dry air for 24 h. **i**, Time-dependent XRD patterns of TEA₂SnI₄ nanoplates with CA stored in dry air for 24 h.

j-m, High-resolution TEM images of perovskite films. Insets: fast Fourier transform diffractograms. Scale bar, 5 nm. To evaluate the surface effect and analysis on how the air-stability relates with crystal stability, we prepared the TEA₂SnI₄ nanoplates with and without CA. From the XPS and XRD results (Extended Data Fig. 5e–i), the TEA₂SnI₄ nanoplates with CA showed less Sn⁴⁺ content, thus proving that CA can enhance the air stability of both perovskite films and nanoplates. From the TEM images (Extended Data Fig. 5j–m), it can be clearly seen that the perovskite with CA still show apparent crystal lattices even after 12 h storage in dry air, indicating the better crystal stability with the introduction of CA.



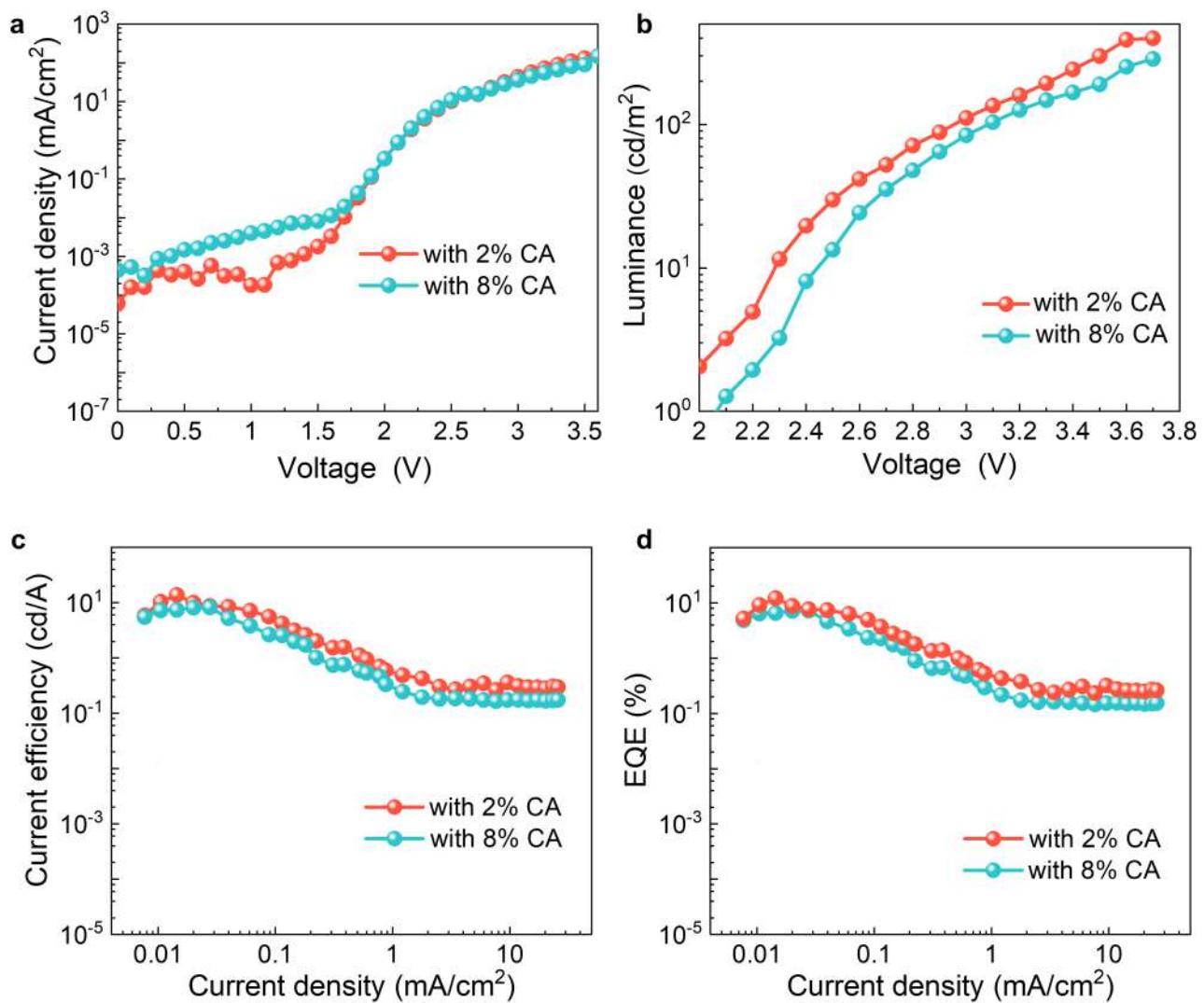
Extended Data Fig. 6 | Optical properties of the Sn perovskite films. **a**, PL spectra of the Sn perovskite films with various CA content. **b**, Logarithm curves of absorption coefficient (α) versus photon energy, the E_U for the pristine and the treated sample are estimated. **c**, Visible absorption spectra of the Sn perovskite films with various CA content. **d**, TRPL spectra of the TEA_2SnI_4 films

prepared with and without 5% CA. **e**, Non-radiative recombination coefficients B for the single-carrier devices with and without CA treatment, the dashed line indicates the condition of room temperature. **f**, Excitation-intensity-dependent PLQYs of the perovskite films with different CA content.



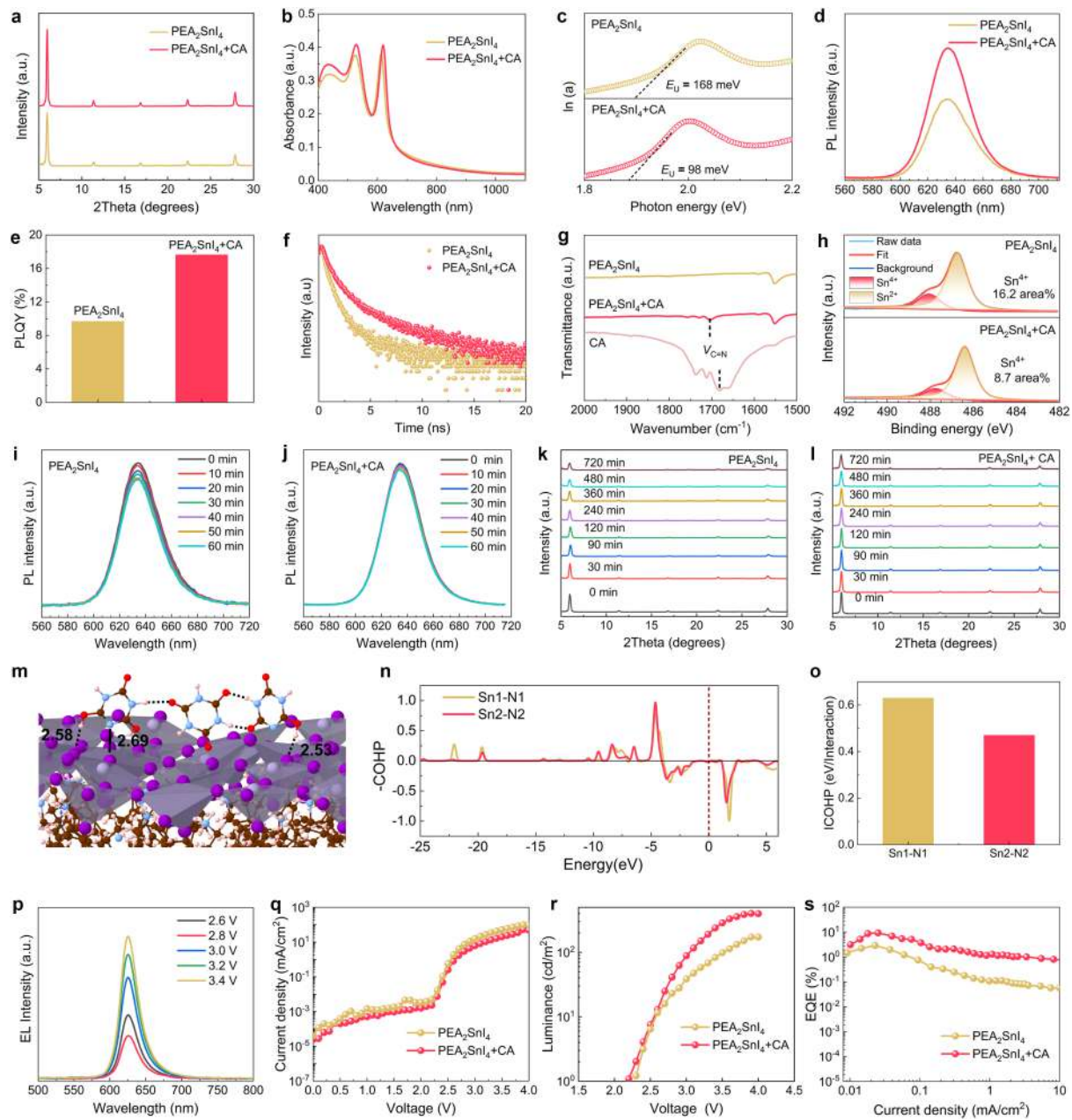
Extended Data Fig. 7 | Photophysical characterization of TEA_2SnI_4 films.
a, The fitted curves of the integrated PL intensity as a function of $1/T$ for the perovskites with and without CA. **b**, Kinetic traces at a probing wavelength of

615 nm for the Sn perovskite films with and without CA. **c, d**, Pseudo-color maps of femtosecond-transient absorption spectra of the pristine (**c**) and the sample with 5% CA (**d**) under an excitation wavelength of 400 nm.



Extended Data Fig. 8 | Device characterization. **a-d**, Device performance for the Sn-PeLEDs with 2% and 8% CA: **(a)** J - V , **(b)** L - V , **(c)** CE - J , and **(d)** EQE - J -curves.

Article



Extended Data Fig. 9 | The efficacy of CA on 2D PEA_2SnI_4 perovskite. **a**, XRD patterns of the perovskite films with and without 5% CA. **b**, Absorption spectra of the perovskite films with and without CA. **c**, Logarithm curves of absorption coefficient (α) versus photon energy, and the Urbach energy (E_U) for the pristine and the treated sample. **d**, PL spectra of the films with and without CA. **e**, PLQYs of the perovskite films with and without CA. **f**, TRPL spectra of the films prepared with and without CA. **g**, FTIR spectra of the PEA_2SnI_4 with and without CA, and the pure CA. **h**, XPS spectra of Sn 3d for the pristine and the CA-treated PEA_2SnI_4 . Time-dependent normalized PL intensity for the pristine (**i**) and the film with CA (**j**) exposed to dry air (20% humidity, RT) for 60 min.

Time-dependent XRD patterns of the pristine (**k**) and the sample with CA (**l**) in dry air for 12 h. **m**, The most stable configurations for the tautomeric CA trimer bonded to the Sn perovskite surface. The distances are in Å. Color code: Sn in grey, I in purple, C in brown, H in pink, O in red, N in blue. **n**, Crystal orbital Hamilton population (COHP) plots of the local Sn-N bond after CA adsorption. **o**, Averaged integrated crystal orbital Hamilton populations (ICOHP) of the Sn-N bonds. **p**, EL spectra of one target device with constant peak emission wavelength of 625 nm under different voltages. **q**, J - V (**q**), L - V (**r**) and EQE/curves (**s**) of the PEA_2SnI_4 based PeLEDs with (9.22%) and without (2.87%) CA.

Extended Data Table 1 | Summary of device performance for recently reported lead-free PeLEDs

No.	Materials	λ_{EL} (nm)	FWHM (nm)	EQE (%)	References
1	CsSnI ₃	950	~80	3.8	Reference 43
2	CH ₃ NH ₃ SnI ₃	945	~60	0.7	Reference 44
3	CsSnBr ₃	672	54	0.3	Reference 45
4	MASnI ₃	901	~80	0.9	Reference 46
5	(PEAI) _{3.5} (CsI) ₅ (SnI ₂) _{4.5}	920	~70	3	Reference 47
6	CsSnBr ₃	674	~45	0.2	Reference 48
7	(PEA) ₂ SnI ₄	633	24	0.30	Reference 20
8	PEA ₂ SnI ₄	632	~30	0.72	Reference 34
9	(PEA) ₂ SnI ₄	630	29	0.52	Reference 35
10	(PEA) ₂ SnI ₄	633	~36	1.48	Reference 49
11	(PEA) ₂ SnI ₄	632	21	5	Reference 16
12	(C ₁₈ H ₃₅ NH ₃) ₂ SnBr ₄	625	162	0.1	Reference 50
13	(BTm) ₂ SnI ₄	627	27.8	3.33	Reference 33
14	(TEA) ₂ SnI ₄	638	32	0.62	Reference 51
15	(TEA) ₂ SnI ₄	638	32	1.37	Reference 32
16	CsSnBr ₃	674	~40	-	Reference 19
17	CsSnI ₃	932	~48	5.4	Reference 18
18	PEAI-FASnI ₃	866	~48	5.3	Reference 17
19	(TEA)₂SnI₄	630	24.9	20.29	This work
20	Cs ₃ Cu ₂ I ₅	438	58	0.1	Reference 52
21	Cs ₃ Cu ₂ I ₅	445	58	1.1	Reference 53
22	CsCu ₂ I ₃	560	180	0.02	Reference 54
23	CsCu ₂ I ₃	550	~120	0.2	Reference 55
24	CsCu ₂ I ₃	568	~120	0.2	Reference 56
25	Cs ₃ Cu ₂ I ₅ :CsCu ₂ I ₃	565	120	3.1	Reference 57
26	TmPyPB-CsCu ₂ I ₃	578	~140	7.4	Reference 56
27	Cs ₃ Sb ₂ Br ₉	408	~60	0.2	Reference 58
28	CsEuBr ₃	448	~30	6.5	Reference 59
29	Cs ₃ CeBr ₆	421	~70	0.5	Reference 60
30	Cs ₃ CeBr _x I _{6-x}	430	-	3.5	Reference 61
31	(ABI) ₄ MnBr ₆	627	45	9.8	Reference 62

λ_{EL} is the peak wavelength of electroluminescent PeLEDs.